Geoscience Frontiers 8 (2017) 1447–1467

HOSTED BY

Contents lists available at ScienceDirect

China University of Geosciences (Beijing)

Geoscience Frontiers

journal homepage: www.elsevier.com/locate/gsf

Research Paper

# Intra-continental back-arc basin inversion and Late Carboniferous magmatism in Eastern Tianshan, NW China: Constraints from the Shaquanzi magmatic suite

Hongjun Jiang [a,b], Jinsheng Han [a,*], Huayong Chen [a,c], Yi Zheng [d], Wanjian Lu [a,b], Gang Deng [e], Zhixiong Tan [e]

[a] Key Laboratory of Mineralogy and Metallogeny, Guangzhou Institute of Geochemistry, Chinese Academy of Sciences, Guangzhou 510640, China
[b] Graduate University of Chinese Academy of Sciences, Beijing 100049, China
[c] Guangdong Provincial Key Laboratory of Mineral Physics and Materials, Guangzhou 510640, China
[d] Department of Earth Sciences, Sun Yat-sen University, Guangzhou 510472, China
[e] No. 6 Geological Party, Xinjiang Bureau of Geology and Mineral Exploration, Hami 839000, China

ARTICLE INFO

*Article history:*
Received 11 April 2016
Received in revised form
22 November 2016
Accepted 11 January 2017
Available online 20 February 2017
Handling Editor: W.J. Xiao

*Keywords:*
Shaquanzi igneous rocks
Geochronology
Geochemistry
Intra-continental back-arc basin
Yamansu belt
Eastern Tianshan Mountains

ABSTRACT

The Yamansu belt, an important tectonic component of Eastern Tianshan Mountains, of the Central Asian Orogenic Belt, NW China hosts many Fe–(Cu) deposit. In this study, we present new zircon U-Pb geochronology and geochemical data of the volcanic rocks of Shaquanzi Formation and diorite intrusions in the Yamansu belt. The Shaquanzi Formation comprises mainly basalt, andesite/andesitic tuff, rhyolite and sub-volcanic diabase with local diorite intrusions. The volcanic rocks and diorites contain ca. 315 −305 Ma and ca. 298 Ma zircons respectively. These rocks show calc-alkaline affinity with enrichment in large-ion lithophile elements (LILEs), light rare-earth elements (LREEs), and depletion in high field strength elements (HFSEs) in primitive mantle normalized multi-element diagrams, which resemble typical back-arc basin rocks. They show depleted mantle signature with $\varepsilon_{Nd}(t)$ ranging from +3.1 to +5.6 for basalt; +2.1 to +4.7 for andesite; −0.2 to +1.5 for rhyolite and the $\varepsilon_{Hf}(t)$ ranges from −0.1 to +13.0 for andesites; +5.8 to +10.7 for andesitic tuffs. We suggest that the Shaquanzi Formation basalt might have originated from a depleted, metasomatized lithospheric mantle source mixed with minor (3–5%) subduction-derived materials, whereas the andesite and rhyolite could be fractional crystallization products of the basaltic magma. The Shaquanzi Formation volcanic rocks could have formed in an intra-continental back-arc basin setting, probably via the southward subduction of the Kangguer Ocean beneath the Middle Tianshan Massif. The Yamansu mineralization belt might have undergone a continental arc to back-arc basin transition during the Late Carboniferous and the intra-continental back-arc basin might have closed in the Early Permian, marked by the emplacement of dioritic magma in the Shaquanzi belt.



## 1. Introduction

The Eastern Tianshan Mountains, located between the Junggar and Tarim blocks, form part of the Central Asian Orogenic Belt (CAOB) (Fig. 1) (Şengör et al., 1993; Xiao et al., 2004, 2013, 2014; Qin et al., 2011; Su et al., 2011). In the region, Carboniferous volcanic rocks and Carboniferous–Permian granitoids are widespread. These rocks are important due to their close proximity to Cu-Au-Fe-Ag mineralization (Zhou et al., 2010; Luo et al., 2012; Zhang et al., 2014; Wang et al., 2015). However, their petrogenesis and tectonic setting are still debated, with various hypotheses proposed including slab subduction (Li, 2004; Xiao et al., 2004, 2014; Hou et al., 2006, 2007; Charvet et al., 2011), intraplate rift (Xiao et al., 1992) and mantle plume-related rifting (Xia et al., 2003, 2012).

The Yamansu belt, an important tectonic component of Eastern Tianshan Mountains, is located between the Middle Tianshan Massif and the Kangguer ductile shear zone (suture zone). Volcanic

* Corresponding author.
*E-mail address:* hanjinsheng@gig.ac.cn (J. Han).
Peer-review under responsibility of China University of Geosciences (Beijing).

http://dx.doi.org/10.1016/j.gsf.2017.01.008

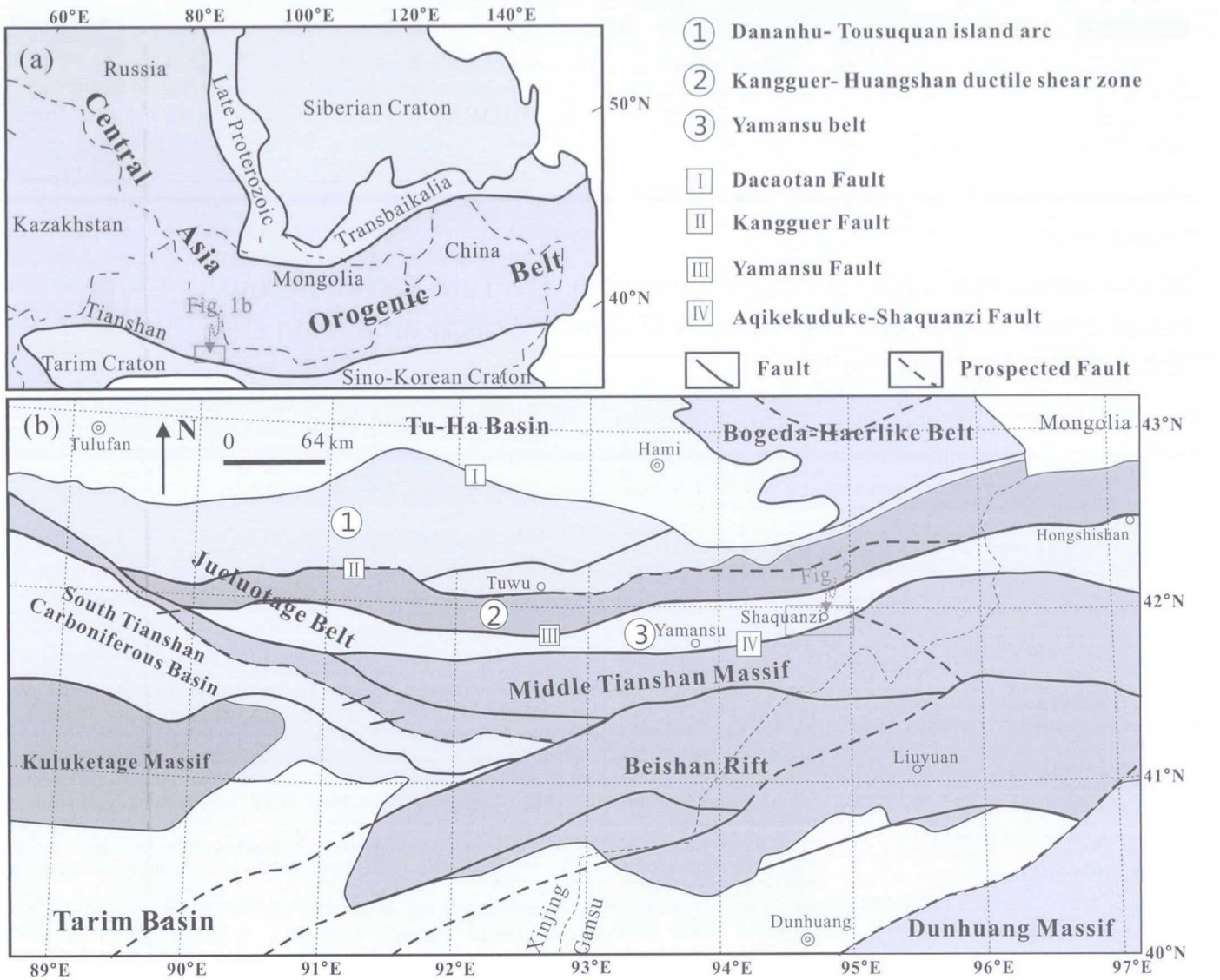


**Figure 1.** (a) Simplified tectonic map of eastern Eurasia, showing the locations of the Siberian, Tarim and Sino-Korean cratons in relation to the Central Asian Orogenic Belt (modified after Su et al., 2011). (b) Regional geologic map of Eastern Tianshan and Beishan Rift (modified after Qin et al., 2002; Su et al., 2011).

rocks of the Lower Carboniferous Yamansu Formation and the Upper Carboniferous Shaquanzi Formation, together with some coeval granitoids, are associated with the Carboniferous Kangguer ocean basin subduction. This makes the Yamansu belt a key area for investigating the tectonic evolution of the Eastern Tianshan Mountains (Yang et al., 1997; Qin et al., 2002; Xiao et al., 2004; Zhou et al., 2010). The Yamansu belt hosts many submarine volcanic-hosted Fe oxide deposits, representing one of the most high-grade Fe resources of China. These deposits include the Yamansu Fe–, Heifengshan Fe–, Shuangfengshan Fe– and Shaquanzi Fe–(Cu) deposits (Huang et al., 2013b; Hou et al., 2014a). Two possible tectonic settings were proposed for these volcanic-hosted Fe–(Cu) deposits, volcanic rocks and granitoids of the Yamansu belt: (1) magmatic arc setting, however, whether it represents island arc (Ma et al., 1993; Xiao et al., 2004) or continental arc (Ji et al., 1994; Yang et al., 1996, 1997; Hou et al., 2006, 2007; Luo et al., 2012; Xu et al., 2014) is debatable; (2) extensional setting, as supported by the presence of marine fossils such as *Dibunophyllum cf.* and *Profusulinella* sp., as well as the Yamansu Formation bimodal volcanic rocks and extension-related mineralization (Qin et al., 2002; Chen et al., 2003; Wang et al., 2006; Hou et al., 2014a). Hou et al. (2014b) proposed that the Yamansu belt was an intra-oceanic back-arc basin, which was related to the Dananhu-Tousuquan island arc, based on geochemistry of the basalt (Lower Carboniferous) from Yamansu Fe deposit. In contrast, Luo et al. (2012) reported that inherited zircons from the felsic rocks of the Yamansu Formation have age peaks (ca. 900 Ma and 1400 Ma) similar to the crystallization ages of the Middle Tianshan Massif, indicating that the Yamansu belt was developed on the Precambrian crystalline basement of the Middle Tianshan Massif. The Upper Carboniferous Shaquanzi Formation, unconformably underlain by the Lower Carboniferous Yamansu Formation comprises mainly intermediate-mafic volcanics rocks. Though several studies presented data on the major, trace geochemistry and platinum-group elements (PGEs) of the volcanic rocks from the Shaquanzi Formation, their petrogenesis and geodynamic background still remain controversial (Li et al., 2011; Huang et al., 2012, 2013a; Xu et al., 2014). In this study, we present zircon U-Pb geochronology, whole-rock geochemistry and Sr-Nd-Pb-Hf isotopes for the Shaquanzi Formation basalt, andesite, rhyolite and the diorite that occur close to the Shaquanzi Fe–(Cu) deposit. Our results, integrated with the published research works on the Yamansu

Formation, suggest a dominantly intra-continental back-arc basin system for the Yamansu mineralization belt during the Late Carboniferous.

## 2. Regional geology

Eastern Tianshan Mountains, in the southern part of the CAOB (Fig. 1a), separates the Tarim Basin to the south and the Junggar Basin to the north (Şengör et al., 1993; Xiao et al., 2004, 2013, 2014; Qin et al., 2011; Su et al., 2011). From north to south, the Eastern Tianshan Mountains comprise three tectonic units: the Bogeda-Haerlike belt, the Jueluotage belt and the Middle Tianshan Massif, which are separated by the Dacaotan and Aqikekuduke-Shaquanzi faults, respectively (Fig. 1b) (Su et al., 2011). The Bogeda-Haerlike belt contains Ordovician–Carboniferous volcanic rocks, granites and mafic-ultramafic complexes (Li, 2004); the Middle Tianshan Massif is composed of a Precambrian crystalline basement of gneiss, schist, migmatite and marble, intruded by calc-alkaline basaltic andesite, volcano-clastics, minor I-type granite and granodiorite (Liu et al., 2004; Mao et al., 2005; Huang et al., 2014a); the Jueluotage belt is characterized by Paleozoic volcano-sedimentary strata, including subaerial volcanics, sandstones and pelitic slates with inter-bedded limestones, mudstones, siltstones and conglomerates, as well as some granitoids and mafic-ultramafic intrusions (Mao et al., 2005). Moreover, the Jueluotage belt can be subdivided, from north to south, into the Dananhu-Tousuquan island arc, Kangguer-Huangshan ductile shear zone and Yamansu belt (Qin et al., 2002; Su et al., 2011) by the approximately EW-trending Kangguer and Yamansu faults (Fig. 1b).

The Dananhu-Tousuquan island arc is represented by basaltic to andesitic volcanic rocks of the Qi'eshan Group, with locally overlying Lower Carboniferous carbonates and calcareous mudstones (Mao et al., 2005). Previous studies show that volcanic rocks of the Qi'eshan Group may have formed in the Carboniferous (ca. 336–320 Ma) (Hou et al., 2005; Li et al., 2005). Overlying the Qi'eshan Group is the Upper Carboniferous Tuwu Formation greywacke, tuff and carbonate interbeds. Volcanic rocks of the Permian Aqikeblak Formation include basalt, tuff, and volcanic breccia. Local outcrops of the Jurassic Xishanyao Formation terrestrial siliciclastics are also present (Mao et al., 2005).

The Kangguer-Huangshan ductile shear zone occurs between the Kangguer and Yamansu faults. The ductile shear zone contains mainly Carboniferous mylonite, tectonic lenses, breccias and a ca. 6–7 km wide belt of fine-grained sandstone and carbonaceous argillites with local bimodal volcanic interbeds (Chen et al., 2003; Mao et al., 2005; Huang et al., 2014a). The sedimentary-volcanic strata were subjected to low-grade metamorphism (Su et al., 2011).

The Yamansu belt, located between the Yamansu and Aqikekuduke-Shaquanzi faults, contains mainly the Yamansu Formation (ca. 5 km thick lower Carboniferous bimodal volcanic sequence), the Shaquanzi Formation (upper Carboniferous intermediate-mafic volcanic lava, pyroclastic rocks, and carbonate rocks), the Tugutublak Formation (clastic rocks, andesitic tuff and intercalated carbonate rocks) and the overlying Lower Permian Aqikebulak Formation marine and terrestrial clastic rocks with intercalated bimodal volcanic rocks and carbonates. Moreover, some Carboniferous marine fossils also occurred in limestone of the Yamansu, Shaquanzi and Tugutublak formations (Chen et al., 2003; Hou et al., 2014b).

Magmatic intrusions along the Jueluotage belt comprise mainly Carboniferous–Permian granitoids (ca. 386–252 Ma) and Permian mafic-ultramafic rocks (ca. 280 Ma; Su et al., 2012). The former includes quartz diorite, granodiorite, granite porphyry, K-feldspar granite and monzogranite (Zhou et al., 2010). The latter is distributed along the northern margin of the Middle Tianshan Massif in the Kanggur-Huangshan ductile shear zone, and contain hornblende/olivine gabbro, (olivine) pyroxenite, pyroxene peridotite and dunite (Qin et al., 2011).

Volcanic rocks from the Shaquanzi Fe–(Cu) deposit in the eastern Yamansu belt are the focus of this study (Fig. 2). They include mainly basalt, andesite, and minor rhyolite, andesitic- and rhyolitic tuff. Sub-volcanic diabase also occurs locally. Diorite, granodiorite and granite are widespread at Shaquanzi, and intrude the Shaquanzi Formation. Some Permian mafic rocks, dominantly

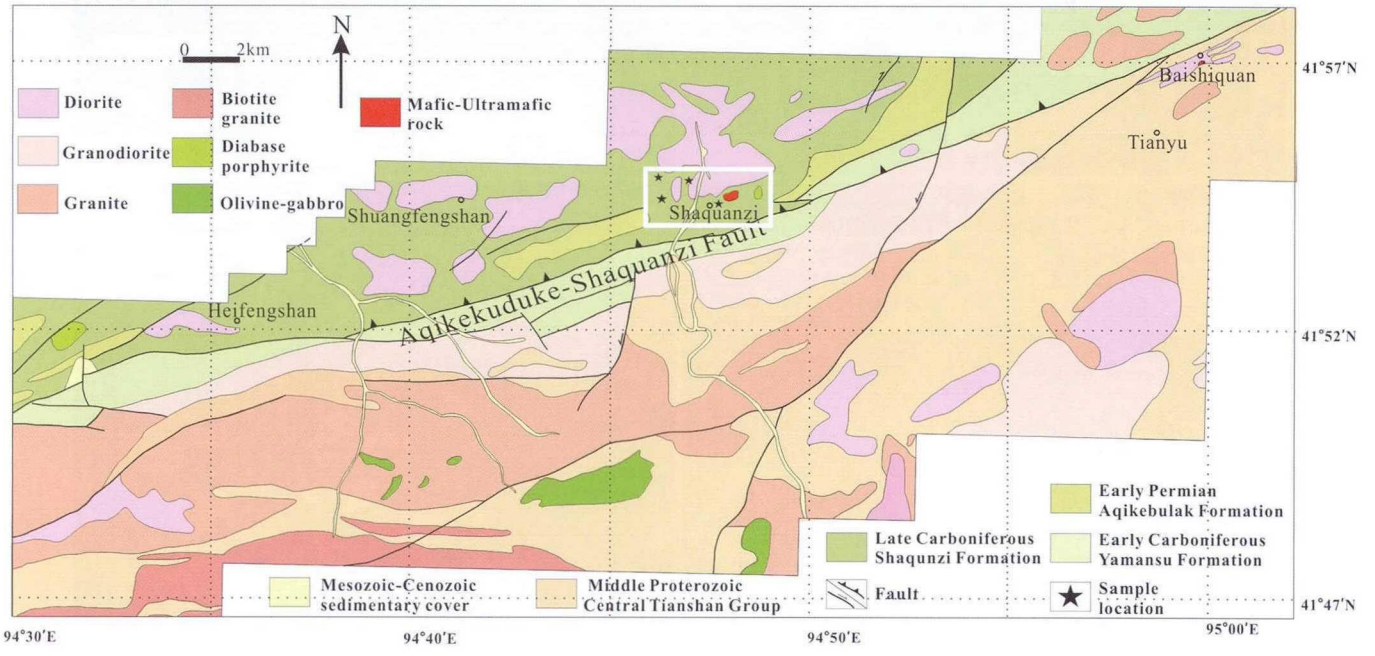


**Figure 2.** Geologic map of the Shaquanzi area (modified after No. 6 Geological Party, Xinjiang Bureau of Geology and Mineral Exploration).

pyroxene diorite, were also observed. The Shaquanzi Fe–(Cu) deposit, hosted in volcanic rocks of the Shaquanzi Formation, is a medium-sized Fe deposit along with significant Cu mineralization. It contains a reserve of 2.49 Mt Fe with grades at 26–49%, and 2040 t Cu with grades at 0.23–1.58%. Ore-forming ages and characteristics of ore-forming fluids were obtained from research of mineral chemistry, isotopes and Re-Os dating of magnetite and pyrite (303 ± 12 Ma and 295 ± 7 Ma, respectively), yet its genesis remains controversial (Hou et al., 2014a; Huang et al., 2014a, b).

## 3. Sampling and petrography

Twenty-one representative volcanic rock samples of the Shaquanzi Formation were collected from the Shaquanzi Fe–(Cu)

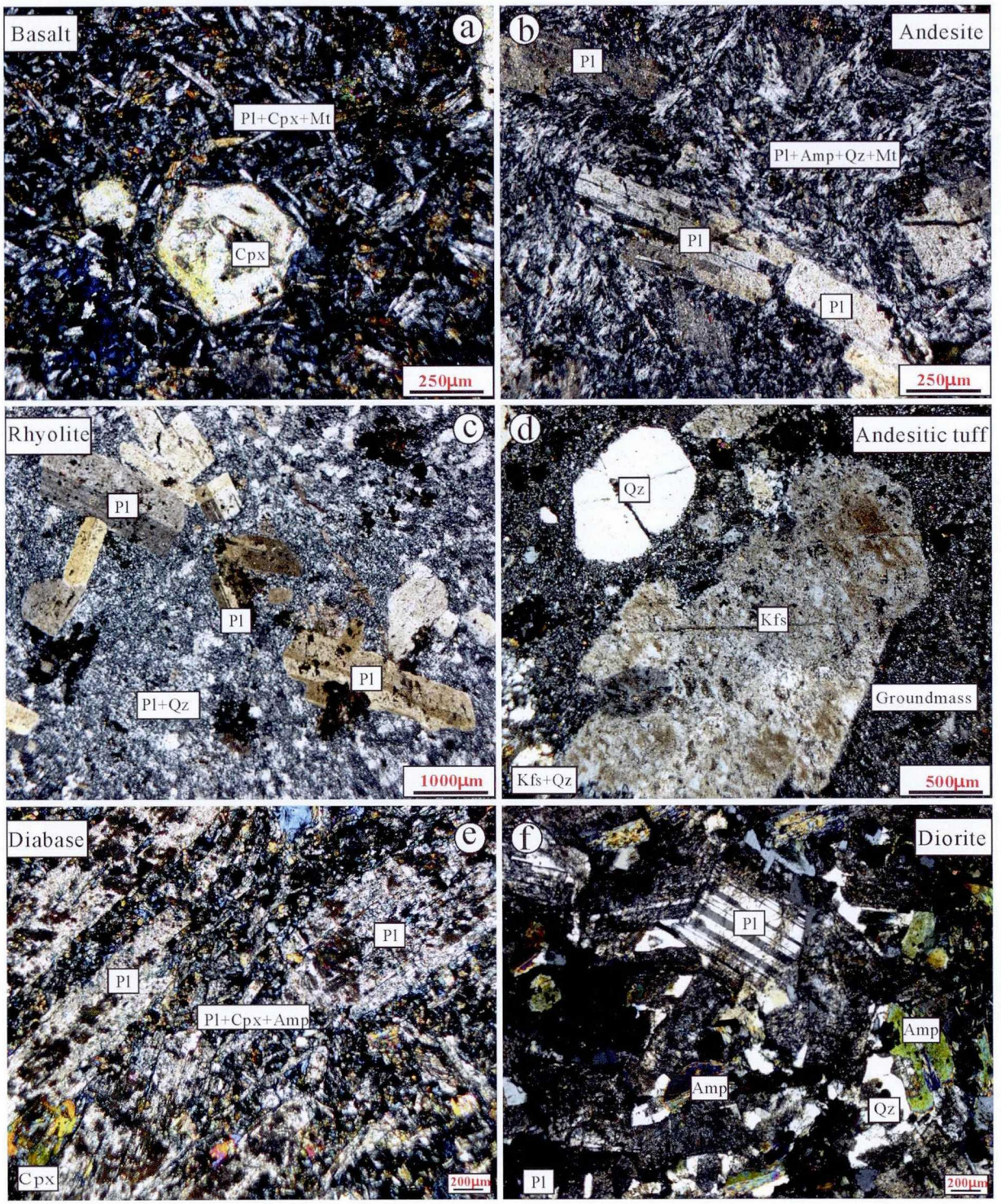


**Figure 3.** Representative photomicrographs for the Shaquanzi Formation volcanic rocks and diorite. (a) Basalt; (b) andesite; (c) rhyolite; (d) andesitic tuff; (e) diabase porphyrite; (f) diorite. Pl = Plagioclase, Kfs = K-feldspar, Qz = Quartz, Cpx = Clinopyroxene, Amp = Amphibole, Mt = Magnetite.

deposit (Fig. 2). These samples cover all lithological types at Shaquanzi, including basalt, andesite (tuff), rhyolite, diabase and diorite. Petrographic observation suggests that these rocks have undergone some alteration and low grade metamorphism, with primary mafic minerals (clinopyroxene and amphibole) replaced by chlorite and feldspar (Fig. 3).

### 3.1. The Shaquanzi Formation volcanic rocks

The basalt displays porphyritic texture and massive structure. The rock contains phenocrysts of clinopyroxene and plagioclase and groundmass of plagioclase, clinopyroxene and minor magnetite (Fig. 3a). The andesite is gray and also shows porphyritic texture and massive structure. The phenocrysts are mainly plagioclase with slight argillic alteration, and the groundmass is dominated by plagioclase, amphibole and cryptocrystalline material showing a typical pilotaxitic texture (Fig. 3b). The rhyolite is light red and displays a porphyritic texture and vesicular structure. The phenocrysts are mainly quartz and minor plagioclase, with a groundmass of plagioclase and quartz (Fig. 3c). The andesitic lithic-crystal tuff is dark gray and consists of ~15% andesite lithic fragments, ~10% crystals (e.g., plagioclase, alkali feldspar and minor quartz), ~70% volcanic ash and ~5% magnetite (Fig. 3d). The diabase porphyrite (sub-volcanic) is greyish-green and contains plagioclase phenocrysts and groundmass (Fig. 3e).

### 3.2. Diorite

The diorite is grayish white and displays fine- to medium-grained hypidiomorphic texture, containing subhedral tabular plagioclase (70–75%), subhedral granular amphibole (20–25%) and minor quartz. Some plagioclase in the diorite display potassic and argillic alteration (Fig. 3f).

## 4. Analytical methods

### 4.1. Whole-rock major-trace elements

Whole-rock major and trace elements analyses were performed at the ALS Chemex Company in Guangzhou, China. A calcined or ignited sample (~0.9 g) is added to ~9.0 g Lithium Borate Flux (50%–50% $Li_2B_4O_7$-$LiBO_2$), mixed well and fused in an auto fluxer between 1050 and 1100 °C. A flat molten glass disk is prepared from the resulting melt. This disk is then analyzed by X-ray fluorescence spectrometry (XRF) for major elements, and the analysis precision is better than ±1–2%. For trace elements, a prepared sample (~0.2 g) is added to lithium metaborate flux (~0.9 g), mixed well and fused in a furnace at 1000 °C. The resulting melt is then cooled and dissolved in 100 mL 4% nitric acid. This solution is then analyzed by inductively coupled plasma-mass spectrometry (ICP-MS) for trace elements. The analytical precision is better than ±5% for most trace elements.

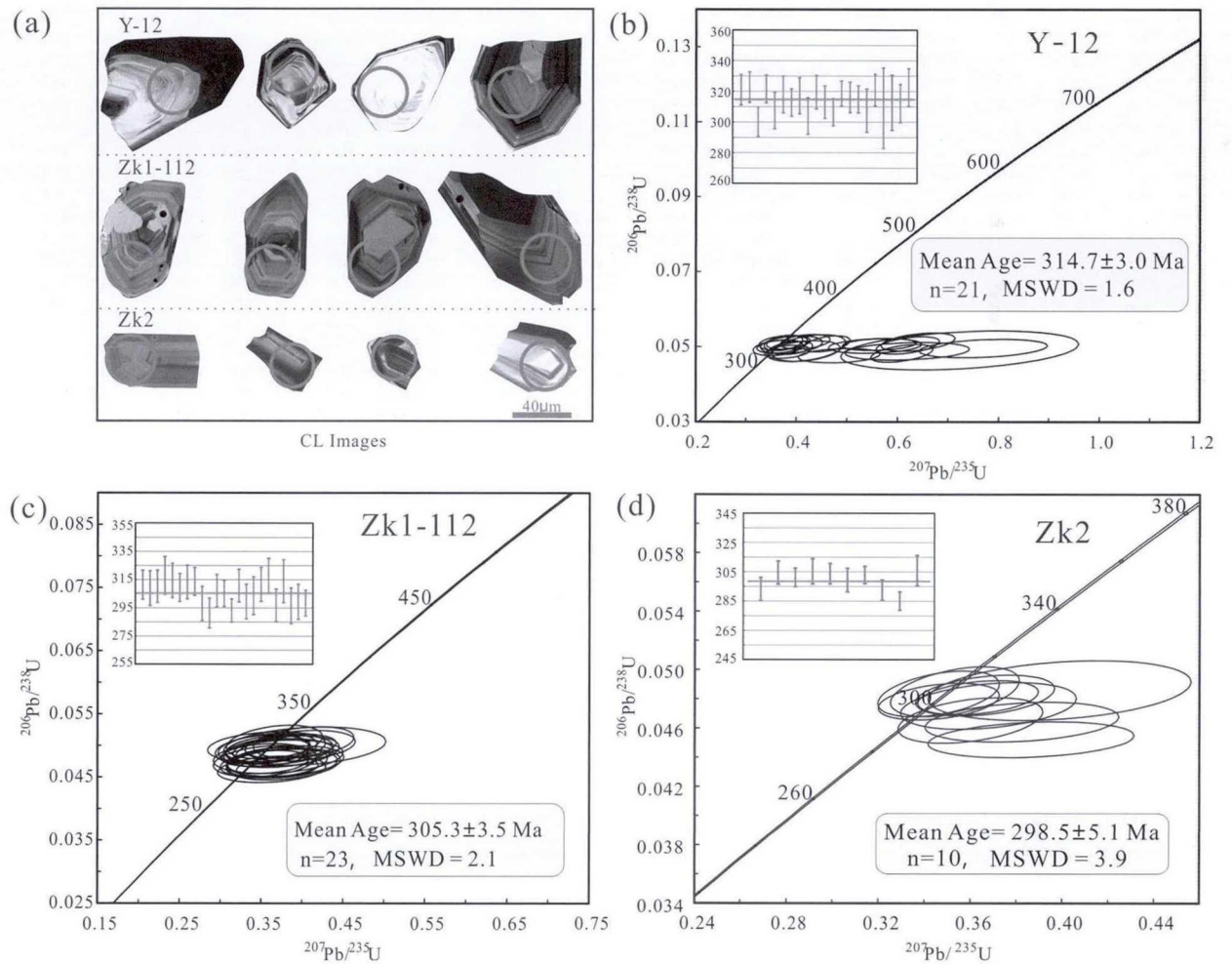


**Figure 4.** (a) Representative cathodoluminescence (CL) images for the analyzed zircons; and zircon U-Pb concordia diagrams for from the Shaquanzi (b) andesite and (c) andesitic tuff and (d) diorite.

**Table 1**
LA-ICP-MS zircon U–Pb dating data for the volcanic rocks and diorite from the Shaquanzi area.

| Sample No. | Th (ppm) | U (ppm) | Pb (ppm) | Th/U | Isotopic ratios | | | | | | Ages (Ma) | | | | | |
|---|---|---|---|---|---|---|---|---|---|---|---|---|---|---|---|---|
| | | | | | $^{207}Pb/^{206}Pb$ | 1σ | $^{207}Pb/^{235}U$ | 1σ | $^{206}Pb/^{238}U$ | 1σ | $^{207}Pb/^{206}Pb$ | 1σ | $^{207}Pb/^{235}U$ | 1σ | $^{206}Pb/^{238}U$ | 1σ |
| Y-12-1 | 89.0 | 155.4 | 0.3 | 0.57 | 0.05264 | 0.00273 | 0.37437 | 0.01981 | 0.05106 | 0.00081 | 322 | 119 | 323 | 15 | 321 | 5 |
| Y-12-2 | 94.9 | 160.9 | 0.9 | 0.59 | 0.05922 | 0.00297 | 0.41752 | 0.02012 | 0.05134 | 0.00081 | 576 | 109 | 354 | 14 | 323 | 5 |
| Y-12-3 | 104.1 | 181.5 | 2.6 | 0.57 | 0.07288 | 0.00461 | 0.48538 | 0.03307 | 0.04765 | 0.00078 | 1011 | 134 | 402 | 23 | 300 | 5 |
| Y-12-4 | 196.9 | 253.2 | 1.7 | 0.78 | 0.05417 | 0.00244 | 0.38436 | 0.01771 | 0.05115 | 0.00073 | 389 | 102 | 330 | 13 | 322 | 5 |
| Y-12-5 | 269.9 | 294.7 | 1.5 | 0.92 | 0.08576 | 0.00535 | 0.61949 | 0.05015 | 0.04886 | 0.00096 | 1333 | 121 | 490 | 31 | 308 | 6 |
| Y-12-7 | 126.4 | 181.8 | 0.8 | 0.70 | 0.05470 | 0.00312 | 0.39040 | 0.02504 | 0.05056 | 0.00097 | 398 | 95 | 335 | 18 | 318 | 6 |
| Y-12-8 | 150.2 | 225.7 | 1.3 | 0.67 | 0.05664 | 0.00234 | 0.39109 | 0.01702 | 0.04971 | 0.00072 | 476 | 91 | 335 | 12 | 313 | 4 |
| Y-12-9 | 97.0 | 172.6 | 1.3 | 0.56 | 0.08995 | 0.00372 | 0.62085 | 0.02554 | 0.05042 | 0.00096 | 1424 | 79 | 490 | 16 | 317 | 6 |
| Y-12-10 | 148.6 | 334.8 | 2.8 | 0.44 | 0.09398 | 0.00458 | 0.60922 | 0.02513 | 0.04828 | 0.00096 | 1509 | 93 | 483 | 16 | 304 | 6 |
| Y-12-11 | 209.5 | 295.1 | 1.5 | 0.71 | 0.06523 | 0.00253 | 0.46110 | 0.01862 | 0.05081 | 0.00088 | 783 | 81 | 385 | 13 | 319 | 5 |
| Y-12-12 | 73.0 | 124.9 | 0.6 | 0.58 | 0.05337 | 0.00308 | 0.36378 | 0.02015 | 0.04975 | 0.00086 | 346 | 134 | 315 | 15 | 313 | 5 |
| Y-12-13 | 126.2 | 186.1 | 0.0 | 0.68 | 0.05640 | 0.00262 | 0.38230 | 0.01843 | 0.04868 | 0.00072 | 478 | 104 | 329 | 14 | 306 | 4 |
| Y-12-14 | 444.3 | 608.3 | 2.6 | 0.73 | 0.07871 | 0.00374 | 0.56434 | 0.02965 | 0.05068 | 0.00066 | 1165 | 62 | 454 | 19 | 319 | 4 |
| Y-12-15 | 432.1 | 460.8 | 6.4 | 0.94 | 0.07951 | 0.00518 | 0.55628 | 0.03758 | 0.05026 | 0.00080 | 1185 | 130 | 449 | 25 | 316 | 5 |
| Y-12-16 | 128.7 | 165.1 | 0.5 | 0.78 | 0.05317 | 0.00275 | 0.36701 | 0.01847 | 0.05005 | 0.00072 | 345 | 119 | 317 | 14 | 315 | 4 |
| Y-12-17 | 38.3 | 66.3 | 0.8 | 0.58 | 0.06473 | 0.00622 | 0.41431 | 0.02956 | 0.04885 | 0.00114 | 765 | 208 | 352 | 21 | 307 | 7 |
| Y-12-18 | 109.9 | 171.9 | 1.2 | 0.64 | 0.05333 | 0.00225 | 0.37489 | 0.01570 | 0.05104 | 0.00084 | 343 | 96 | 323 | 12 | 321 | 5 |
| Y-12-19 | 421.2 | 470.5 | 1.1 | 0.90 | 0.10515 | 0.01250 | 0.72370 | 0.09610 | 0.04910 | 0.00213 | 1717 | 220 | 553 | 57 | 309 | 13 |
| Y-12-20 | 70.1 | 124.0 | 0.2 | 0.56 | 0.06434 | 0.00665 | 0.42505 | 0.02979 | 0.04970 | 0.00146 | 754 | 225 | 360 | 21 | 313 | 9 |
| Y-12-21 | 587.7 | 513.9 | 7.5 | 1.14 | 0.10948 | 0.00624 | 0.77030 | 0.05188 | 0.04962 | 0.00101 | 1791 | 104 | 580 | 30 | 312 | 6 |
| Y-12-23 | 243.7 | 404.5 | 6.8 | 0.60 | 0.07875 | 0.00443 | 0.64097 | 0.02977 | 0.05130 | 0.00100 | 1166 | 112 | 503 | 18 | 323 | 6 |
| ZK1-112-1 | 97.0 | 103.3 | 0.1 | 0.94 | 0.05276 | 0.00317 | 0.35871 | 0.02107 | 0.04948 | 0.00084 | 317 | 137 | 311 | 16 | 311 | 5 |
| ZK1-112-2 | 38.9 | 57.6 | 0.6 | 0.68 | 0.05709 | 0.00419 | 0.38241 | 0.02580 | 0.04909 | 0.00100 | 494 | 163 | 329 | 19 | 309 | 6 |
| ZK1-112-4 | 28.1 | 49.9 | 1.0 | 0.56 | 0.05686 | 0.00441 | 0.37669 | 0.02495 | 0.04930 | 0.00093 | 487 | 172 | 325 | 18 | 310 | 6 |
| ZK1-112-5 | 44.6 | 64.9 | 0.4 | 0.69 | 0.05325 | 0.00386 | 0.36635 | 0.02398 | 0.05055 | 0.00109 | 339 | 165 | 317 | 18 | 318 | 7 |
| ZK1-112-7 | 26.9 | 46.8 | 0.4 | 0.58 | 0.05927 | 0.00507 | 0.39804 | 0.02752 | 0.04998 | 0.00099 | 576 | 182 | 340 | 20 | 314 | 6 |
| ZK1-112-8 | 44.0 | 66.1 | 0.0 | 0.67 | 0.05312 | 0.00341 | 0.35853 | 0.02116 | 0.04917 | 0.00081 | 345 | 142 | 311 | 16 | 309 | 5 |
| ZK1-112-9 | 22.7 | 41.1 | 0.4 | 0.55 | 0.05312 | 0.00522 | 0.35672 | 0.02952 | 0.04981 | 0.00097 | 345 | 224 | 310 | 22 | 313 | 6 |
| ZK1-112-10 | 53.6 | 79.8 | 1.2 | 0.67 | 0.05671 | 0.00351 | 0.38628 | 0.02271 | 0.04988 | 0.00080 | 480 | 134 | 332 | 17 | 314 | 5 |
| ZK1-112-11 | 38.6 | 63.1 | 0.1 | 0.61 | 0.05846 | 0.00450 | 0.36947 | 0.02528 | 0.04732 | 0.00098 | 546 | 169 | 319 | 19 | 298 | 6 |
| ZK1-112-13 | 86.0 | 95.5 | 0.4 | 0.90 | 0.05796 | 0.00459 | 0.36299 | 0.02711 | 0.04623 | 0.00086 | 528 | 174 | 314 | 20 | 291 | 5 |
| ZK1-112-14 | 21.2 | 42.9 | 0.1 | 0.49 | 0.05653 | 0.00457 | 0.37127 | 0.02721 | 0.04880 | 0.00093 | 472 | 180 | 321 | 20 | 307 | 6 |
| ZK1-112-15 | 85.6 | 92.5 | 1.3 | 0.93 | 0.05309 | 0.00359 | 0.35364 | 0.02175 | 0.04848 | 0.00074 | 332 | 154 | 307 | 16 | 305 | 5 |
| ZK1-112-16 | 249.1 | 270.8 | 0.6 | 0.92 | 0.05746 | 0.00308 | 0.36995 | 0.02043 | 0.04651 | 0.00067 | 509 | 123 | 320 | 15 | 293 | 4 |
| ZK1-112-17 | 64.0 | 76.5 | 0.3 | 0.84 | 0.05276 | 0.00380 | 0.35071 | 0.02329 | 0.04938 | 0.00094 | 317 | 165 | 305 | 18 | 311 | 6 |
| ZK1-112-20 | 35.4 | 53.1 | 0.0 | 0.67 | 0.05937 | 0.00526 | 0.37953 | 0.02930 | 0.04754 | 0.00099 | 589 | 193 | 327 | 22 | 299 | 6 |
| ZK1-112-21 | 36.2 | 51.6 | 0.9 | 0.70 | 0.05540 | 0.00489 | 0.37077 | 0.03241 | 0.04822 | 0.00108 | 428 | 196 | 320 | 24 | 304 | 7 |
| ZK1-112-22 | 42.5 | 59.9 | 0.9 | 0.71 | 0.05372 | 0.00464 | 0.35807 | 0.02476 | 0.04954 | 0.00098 | 367 | 196 | 311 | 19 | 312 | 6 |
| ZK1-112-23 | 38.0 | 56.4 | 1.3 | 0.67 | 0.06101 | 0.00437 | 0.40218 | 0.02504 | 0.05050 | 0.00102 | 639 | 156 | 343 | 18 | 318 | 6 |
| ZK1-112-25 | 32.1 | 51.6 | 0.1 | 0.62 | 0.05745 | 0.00497 | 0.37163 | 0.02930 | 0.04712 | 0.00094 | 509 | 191 | 321 | 22 | 297 | 6 |
| ZK1-112-26 | 31.7 | 45.9 | 1.6 | 0.69 | 0.06087 | 0.00654 | 0.40337 | 0.04047 | 0.04991 | 0.00124 | 635 | 233 | 344 | 29 | 314 | 8 |
| ZK1-112-27 | 30.6 | 51.9 | 0.0 | 0.59 | 0.06038 | 0.00518 | 0.37729 | 0.02848 | 0.04706 | 0.00103 | 617 | 186 | 325 | 21 | 296 | 6 |
| ZK1-112-28 | 38.8 | 55.7 | 0.0 | 0.70 | 0.05515 | 0.00430 | 0.35485 | 0.02592 | 0.04753 | 0.00101 | 417 | 174 | 308 | 19 | 299 | 6 |
| ZK1-112-29 | 163.4 | 147.1 | 0.3 | 1.11 | 0.05460 | 0.00306 | 0.35870 | 0.02027 | 0.04739 | 0.00075 | 394 | 126 | 311 | 15 | 298 | 5 |
| ZK2-3 | 588.9 | 688.2 | 2.0 | 0.86 | 0.05666 | 0.00233 | 0.36009 | 0.01285 | 0.04653 | 0.00064 | 480 | 93 | 312 | 10 | 293 | 4 |
| ZK2-6 | 2931.8 | 2019.9 | 0.0 | 1.45 | 0.05201 | 0.00164 | 0.34629 | 0.01073 | 0.04782 | 0.00051 | 287 | 77 | 302 | 8 | 301 | 3 |
| ZK2-7 | 1279.6 | 1368.5 | 1.3 | 0.94 | 0.05138 | 0.00175 | 0.35331 | 0.01143 | 0.04850 | 0.00070 | 257 | 78 | 307 | 9 | 305 | 4 |
| ZK2-9 | 619.3 | 627.6 | 1.0 | 0.99 | 0.05522 | 0.00187 | 0.36646 | 0.01237 | 0.04824 | 0.00057 | 420 | 76 | 317 | 9 | 304 | 4 |
| ZK2-11 | 1870.0 | 1728.1 | 0.8 | 1.08 | 0.05500 | 0.00209 | 0.36792 | 0.01561 | 0.04753 | 0.00065 | 413 | 85 | 318 | 12 | 299 | 4 |
| ZK2-13 | 448.4 | 683.5 | 1.0 | 0.66 | 0.05530 | 0.00175 | 0.36339 | 0.01072 | 0.04809 | 0.00048 | 433 | 70 | 315 | 8 | 303 | 3 |
| ZK2-14 | 809.1 | 748.8 | 1.3 | 1.08 | 0.05971 | 0.00249 | 0.38251 | 0.01722 | 0.04642 | 0.00056 | 594 | 89 | 329 | 13 | 292 | 3 |
| ZK2-18 | 1352.4 | 1118.6 | 2.7 | 1.21 | 0.06155 | 0.00278 | 0.38652 | 0.01830 | 0.04521 | 0.00050 | 657 | 94 | 332 | 13 | 285 | 3 |
| ZK2-19 | 118.2 | 135.1 | 0.0 | 0.87 | 0.06030 | 0.00356 | 0.39902 | 0.02343 | 0.04858 | 0.00084 | 613 | 128 | 341 | 17 | 306 | 5 |

### 4.2. Whole-rock Sr-Nd-Pb isotopes

Whole-rock Sr-Nd-Pb isotopic analyses were performed by using a Micromass Isoprobe Multi-Collector (MC)-ICPMS at the Guangzhou institute of Geochemistry (GIGCAS), China. For Sr-Nd isotopic analyses, sample powders (~100 mg) were dissolved in distilled HF-$HNO_3$ Savillex screw-top Teflon beakers at 150 °C overnight. Strontium and REEs were separated on columns made of Sr and REE resins from the Eichrom Company using 0.1% $HNO_3$ as eluant. Separation of Nd from the REE fractions was carried out on HDEHP columns with a 0.18 N HCl eluant. Measured Sr and Nd isotopic ratios were normalized using $^{86}Sr/^{88}Sr$ value of 0.1194 and $^{146}Nd/^{144}Nd$ value of 0.7219, respectively. Analyses of standards NIST SRM, and Jndi-1 over the measurement period provided $^{87}Sr/^{86}Sr = 0.710291 \pm 6\ (2\sigma)$, and $^{143}Nd/^{144}Nd = 0.512084 \pm 3\ (2\sigma)$, respectively. For Pb analyses, ~200 mg powder was dissolved in concentrated HF for three days. Pb was separated and purified by conventional cation-exchange techniques (200–400 mesh AG1X8 resin) with diluted HBr as eluant. Analyses of standard NBS981 during the period of analysis provide $^{206}Pb/^{204}Pb = 16.9319 \pm 3$, $^{207}Pb/^{204}Pb = 15.4849 \pm 3$, and $^{208}Pb/^{204}Pb = 36.6781 \pm 11$ (Xu et al., 2012).

### 4.3. Zircon U-Pb geochronology and in-situ Hf isotopes

Zircon grains were separated by the standard density and magnetic separation techniques, and then hand-picked under a binocular microscope. To study the zircon internal structure,

cathodoluminescence (CL) imaging was carried out using a JXA-8100 Electron Probe Microanalyzer (EPMA) with a Mono CL3 Cathodoluminescence System for high resolution imaging and spectroscopy at the GIGCAS.

LA-ICP-MS zircons and U-Pb dating samples were performed at the GIGCAS. The clearest and least fractured rims of the zircon crystals were selected for laser ablation. U-Pb dating and trace element analyses were conducted synchronously using LA-ICP-MS. Sample mounts were placed in a special sample cell designed by Laurin Technic Pty. Ltd, flushed with Ar and He. Laser ablation was accomplished using a pulsed Resonetic 193 nm ArF excimer laser, operated at a constant energy of 80 mJ, with a repetition rate of 8 Hz and a spot diameter of 31 μm. The ablated aerosol was carried to an Agilent 7500a ICP-MS by He gas via a Squid system to smooth signals (Liang et al., 2009; Tu et al., 2011; Li et al., 2012). Data were acquired for 30 s with the laser off, and 40 s with the laser on, giving approximately 100 mass scans. NIST SRM 610 glass (Pearce et al., 1997; Gao et al., 2002) and Temora zircon standards (Black et al., 2003) were used as external standards. Each block of five unknowns was bracketed by analyses of standards. Off-line inspection and integration of background and analyze signals, and time-drift correction and quantitative calibration for trace element analyses and U-Pb dating were performed using ICPMS Data Cal (Liu et al., 2008, 2010). Concordia diagrams and weighted mean calculations were made using Isoplot/Ex_ver3 (Ludwig, 2003). A more detailed analytical technique was described in Yuan et al. (2004).

*In-situ* zircon Lu-Hf isotopic measurements were undertaken using the Nu plasma high resolution (HR) MC-ICP-MS, equipped with a Geolas 193 nm ArF Excimer laser in selected dated zircon grains at the GIGCAS. The measured isotopic ratios of $^{176}Hf/^{177}Hf$ were normalized to $^{179}Hf/^{177}Hf = 0.7325$, using exponential correction for mass bias. The *in-situ* measured $^{173}Yb/^{172}Yb$ ratio was used for mass bias correction for both Yb and Lu because of their similar physicochemical properties. Ratios used for the corrections were 0.5886 for $^{176}Yb/^{172}Yb$ (Chu et al., 2002) and 0.02655 for $^{176}Lu/^{175}Lu$ (Machado and Simonetti, 2001). The measured $^{176}Lu/^{177}Hf$ ratios and the $^{176}Lu$ decay constant of $1.867 \times 10^{-11}$ year$^{-1}$ reported by Soderlund et al. (2004) were used to calculate the initial $^{176}Hf/^{177}Hf$ ratios. Chondritic values of $^{176}Hf/^{177}Hf = 0.0336$ and $^{176}Lu/^{177}Hf = 0.282785$ reported by Bouvier et al. (2008) were used for the calculation of $\varepsilon_{Hf}(t)$ values. The depleted mantle line is defined by present-day $^{176}Hf/^{177}Hf = 0.28325$ and $^{176}Lu/^{177}Hf = 0.0384$ (Griffin et al., 2000). Single-stage Hf model ages ($T_{DM1}$) were calculated relative to the depleted mantle which is assumed to have linear isotopic growth from $^{176}Hf/^{177}Hf = 0.279718$ at 4.55 Ga, to 0.283250 at present, with a $^{176}Lu/^{177}Hf = 0.0384$ (Griffin et al., 2000), and two-stage Hf model ages ($T_{DM2}$) were calculated assuming a mean $^{76}Lu/^{177}Hf$ value of 0.015 for the average continental crust (Griffin et al., 2002).

## 5. Results

### 5.1. Zircon U-Pb ages

Zircons from andesite (sample Y-12), andesitic tuff (sample ZK1-112) and diorite (sample ZK2) of the Shaquanzi Formation were studied by CL imaging (Fig. 4a) and U-Pb dating (Fig. 4b–d) (Table 1). All analyzed zircons are euhedral-subhedral with igneous oscillatory zoning (Fig. 4a). They contain high Th/U (0.44–3.86; except for one discordant spot (8.12); Table 1), indicating their magmatic origin (Koschek, 1993).

Zircon grains in the andesite (sample Y-12) (Fig. 3b) yield a weighted mean age of 314.7 ± 3.0 Ma (MSWD = 1.6, $n$ = 21) (Fig. 4b). One older grain with an age of ca. 394 Ma is interpreted to be inherited. Andesitic tuff (sample ZK1-112) (Fig. 3d) yields a weighted mean age of 305.3 ± 3.5 Ma (MSWD = 2.1, $n$ = 23) (Fig. 4c). The diorite (sample ZK2) (Fig. 3f) yields a weighted mean age of 298.5 ± 5.1 Ma (MSWD = 3.9, $n$ = 10) (Fig. 4d). There are three inherited zircons with ages ranging from ca. 443 Ma to 483 Ma.

### 5.2. Whole-rock geochemistry

As stated above, the rocks have undergone some alteration and low grade metamorphism, with primary mafic minerals (clinopyroxene and amphibole) replaced by chlorite and feldspar. Thus in the $SiO_2$ vs. Nb/Y diagram (Fig. 5a), most samples are subalkaline and plotted in the basalt, andesite and rhyolitic dacite fields. The rocks display mainly calc-alkaline affinity in the Th vs. Co diagram (Fig. 5b). Moreover, Fe, Ti, Al, Mg, Ca and P exhibit good linear relationships with $SiO_2$ in the Harker diagram (Appendix 1).

As shown in Table 2, the basalt and diabase porphyrite show similar geochemical characteristics. Both rock types have

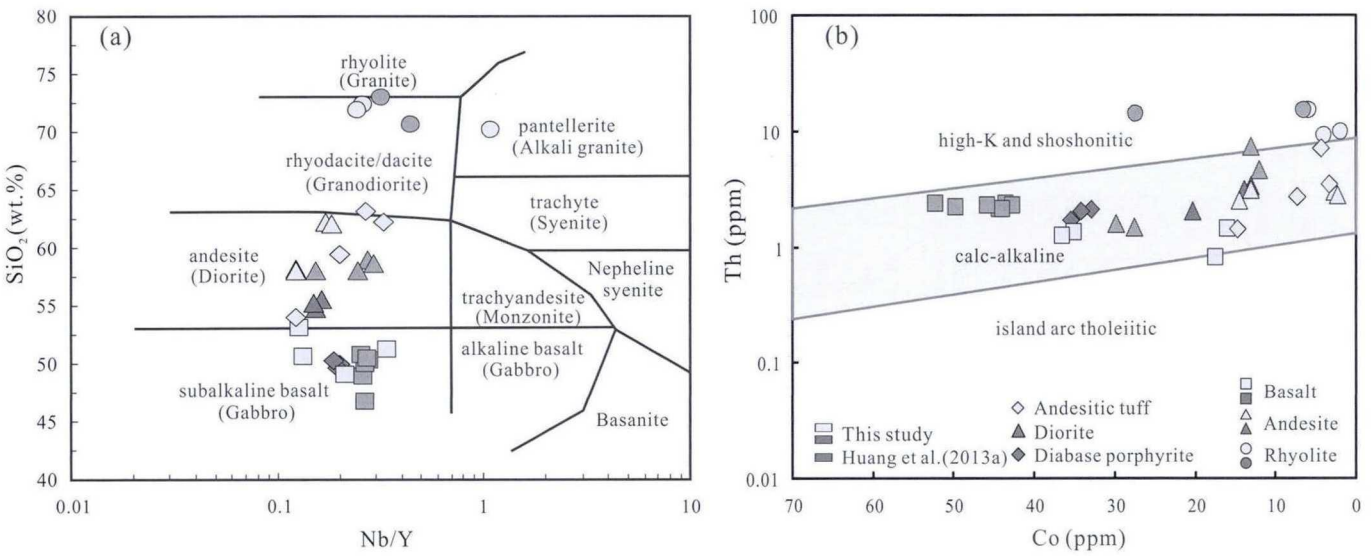


**Figure 5.** $SiO_2$ vs. Nb/Y diagram (Winchester and Floyd, 1977); (b) Th vs. Co diagram (Hastie et al., 2007).

**Table 2**
Major (wt.%) and trace (ppm) element compositions for the volcanic rocks and diorite from Shaquanzi.

| Sample No. | ZK2-12 | ZK5-1 | ZK5-6 | ZK6-3 | ZK6-4 | ZK6-5 | ZK2-15 | ZK2-16 | ZK1-76 | ZK1-99 | Y-05 | Y-12 | ZK1-77 | ZK1-79 | ZK1-28 | ZK1-31 | ZK1-87 | ZK1-112 | SY-08 | SY-39 | ZK1-48 |
|---|---|---|---|---|---|---|---|---|---|---|---|---|---|---|---|---|---|---|---|---|---|
| Rock type | Diorite | | | Diabase | | | Basalt | | | | Andesite | | | | Andesitic tuff | | | | Rhyolite | | |
| **Major element** | | | | | | | | | | | | | | | | | | | | | |
| $SiO_2$ | 53.95 | 53.56 | 53.75 | 48.13 | 47.53 | 48.41 | 49.30 | 46.98 | 49.21 | 51.99 | 60.39 | 60.42 | 57.51 | 56.87 | 58.31 | 61.83 | 52.98 | 61.09 | 66.75 | 70.47 | 70.87 |
| $TiO_2$ | 0.76 | 0.87 | 0.88 | 1.11 | 1.16 | 1.12 | 1.86 | 1.39 | 0.78 | 0.86 | 0.66 | 0.63 | 1.18 | 1.21 | 0.85 | 0.84 | 0.78 | 0.53 | 0.10 | 0.42 | 0.37 |
| $Al_2O_3$ | 17.69 | 16.78 | 17.03 | 17.04 | 17.30 | 17.14 | 15.59 | 16.65 | 18.32 | 18.56 | 16.78 | 16.66 | 14.62 | 14.62 | 17.16 | 16.32 | 16.70 | 18.03 | 9.91 | 14.60 | 13.52 |
| $Fe_2O_3$ | 8.31 | 8.86 | 8.63 | 10.40 | 10.36 | 10.17 | 9.64 | 10.74 | 10.12 | 8.80 | 3.29 | 3.53 | 11.74 | 10.95 | 6.67 | 5.02 | 13.03 | 5.30 | 7.03 | 1.53 | 3.36 |
| MnO | 0.15 | 0.17 | 0.14 | 0.17 | 0.17 | 0.17 | 0.14 | 0.17 | 0.20 | 0.21 | 0.10 | 0.11 | 0.16 | 0.14 | 0.15 | 0.13 | 0.13 | 0.12 | 0.60 | 0.07 | 0.07 |
| MgO | 4.31 | 4.02 | 4.53 | 5.95 | 4.85 | 5.84 | 6.38 | 6.11 | 5.19 | 3.36 | 1.78 | 1.48 | 3.18 | 2.66 | 3.08 | 1.88 | 3.26 | 2.58 | 3.95 | 0.43 | 1.66 |
| CaO | 7.25 | 6.73 | 5.45 | 9.32 | 10.37 | 9.11 | 7.92 | 9.97 | 7.08 | 7.10 | 3.96 | 3.98 | 2.92 | 2.66 | 3.42 | 2.17 | 2.61 | 2.29 | 3.60 | 1.96 | 1.40 |
| $Na_2O$ | 2.92 | 3.72 | 3.73 | 2.48 | 2.73 | 2.45 | 3.47 | 2.56 | 2.65 | 4.46 | 5.59 | 5.34 | 5.56 | 3.49 | 5.04 | 2.95 | 4.75 | 6.69 | 1.53 | 7.47 | 5.14 |
| $K_2O$ | 1.50 | 2.79 | 2.93 | 1.28 | 0.79 | 1.40 | 1.34 | 0.94 | 3.53 | 2.50 | 4.06 | 4.96 | 1.45 | 5.08 | 3.12 | 6.58 | 3.60 | 1.46 | 1.68 | 0.42 | 2.08 |
| $P_2O_5$ | 0.146 | 0.266 | 0.284 | 0.328 | 0.357 | 0.336 | 0.529 | 0.318 | 0.181 | 0.231 | 0.289 | 0.283 | 0.351 | 0.349 | 0.217 | 0.210 | 0.177 | 0.082 | 0.011 | 0.092 | 0.074 |
| LOI | 2.59 | 1.93 | 1.92 | 3.10 | 3.63 | 3.01 | 3.14 | 3.57 | 2.55 | 1.32 | 1.95 | 1.84 | 1.05 | 1.11 | 1.10 | 1.41 | 1.44 | 1.53 | 3.82 | 1.53 | 1.03 |
| Total | 99.58 | 99.70 | 99.27 | 99.31 | 99.25 | 99.16 | 99.31 | 99.40 | 99.81 | 99.39 | 98.85 | 99.23 | 99.72 | 99.14 | 99.12 | 99.34 | 99.46 | 99.70 | 98.98 | 98.99 | 99.57 |
| Mg# | 54.72 | 51.40 | 55.02 | 57.14 | 52.18 | 57.23 | 60.67 | 57.00 | 54.45 | 47.09 | 55.77 | 49.42 | 38.70 | 36.15 | 51.83 | 46.60 | 36.83 | 53.15 | 56.70 | 39.58 | 53.52 |
| **Trace element** | | | | | | | | | | | | | | | | | | | | | |
| Li | 11.1 | 6.8 | 10.2 | 15.3 | 14.4 | 15.7 | 16.9 | 14.7 | 27.1 | 15.0 | 8.5 | 5.7 | 13.7 | 11.4 | 16.6 | 12.1 | 14.2 | 15.3 | 14.2 | 4.5 | 14.5 |
| Be | 0.59 | 0.79 | 0.88 | 0.96 | 1.12 | 0.96 | 1.21 | 0.75 | 0.62 | 0.62 | 1.13 | 1.02 | 0.84 | 0.68 | 1.10 | 1.32 | 0.67 | 1.29 | 0.33 | 0.94 | 1.16 |
| Sc | 23.3 | 28.7 | 26.5 | 25.1 | 27.8 | 25.8 | 22.9 | 27.5 | 27.6 | 24.4 | 15.4 | 14.8 | 31.6 | 29.0 | 26.7 | 13.6 | 23.3 | 14.1 | 4.0 | 10.4 | 10.2 |
| P | 640 | 1200 | 1240 | 1460 | 1600 | 1470 | 2380 | 1410 | 800 | 990 | 1270 | 1250 | 1550 | 1510 | 950 | 930 | 780 | 360 | 50 | 390 | 330 |
| Ti | 4220 | 4740 | 4210 | 6510 | 6920 | 6630 | 11,100 | 8070 | 4440 | 4750 | 3710 | 3740 | 6820 | 6630 | 4910 | 4750 | 4420 | 3050 | 670 | 2430 | 2320 |
| V | 227 | 257 | 258 | 261 | 265 | 261 | 210 | 286 | 289 | 254 | 66 | 69 | 234 | 220 | 182 | 89 | 262 | 80 | 8 | 16 | 39 |
| Cr | 21 | 33 | 26 | 78 | 78 | 73 | 168 | 56 | 30 | 5 | 24 | 27 | 7 | 5 | 59 | 16 | 9 | 8 | 21 | 48 | 13 |
| Mn | 1100 | 1270 | 1040 | 1260 | 1260 | 1240 | 1040 | 1240 | 1480 | 1500 | 776 | 807 | 1230 | 1040 | 1100 | 949 | 950 | 844 | 4590 | 474 | 494 |
| Co | 20.5 | 13.2 | 14.1 | 35.6 | 33.0 | 34.2 | 35.1 | 36.5 | 17.5 | 16.2 | 2.9 | 2.5 | 13.3 | 14.7 | 7.5 | 4.6 | 14.9 | 3.6 | 5.9 | 2.1 | 4.2 |
| Ni | 13.4 | 13.5 | 10.7 | 42.4 | 37.6 | 39.1 | 113.0 | 42.1 | 15.2 | 4.6 | 1.2 | 1.0 | 1.5 | 1.2 | 12.9 | 4.9 | 6.7 | 3.1 | 2.4 | 2.0 | 5.0 |
| Cu | 69.0 | 53.5 | 40.3 | 68.0 | 86.7 | 76.8 | 53.8 | 87.7 | 66.3 | 63.1 | 32.1 | 20.6 | 8.1 | 9.3 | 13.7 | 5.5 | 4.4 | 11.8 | 4.0 | 13.8 | 2.3 |
| Zn | 77 | 63 | 69 | 97 | 98 | 96 | 101 | 86 | 150 | 199 | 46 | 40 | 89 | 65 | 273 | 43 | 109 | 100 | 316 | 31 | 40 |
| Ga | 18.70 | 18.85 | 18.45 | 20.8 | 22.6 | 20.5 | 20.5 | 19.80 | 19.30 | 18.80 | 19.45 | 18.55 | 18.80 | 15.90 | 20.0 | 15.80 | 16.35 | 19.25 | 8.24 | 14.20 | 15.40 |
| Rb | 13.9 | 53.0 | 40.7 | 17.2 | 8.8 | 25.5 | 18.9 | 7.8 | 48.8 | 55.5 | 67.5 | 81.7 | 66.9 | 123.5 | 97.2 | 158.0 | 80.2 | 48.2 | 31.2 | 16.7 | 77.5 |
| Sr | 415 | 458 | 404 | 515 | 621 | 513 | 500 | 624 | 376 | 446 | 349 | 285 | 159.5 | 197.5 | 273 | 315 | 263 | 281 | 134.5 | 113.0 | 194.0 |
| Y | 16.3 | 21.3 | 18.1 | 18.8 | 21.9 | 20.4 | 24.5 | 20.8 | 12.6 | 16.2 | 24.2 | 23.0 | 32.5 | 29.8 | 22.1 | 32.8 | 18.7 | 15.6 | 9.2 | 28.2 | 29.9 |
| Zr | 61.4 | 64.2 | 65.6 | 112.5 | 122.5 | 117.5 | 146.0 | 89.4 | 18.6 | 35.2 | 115.0 | 112.5 | 64.0 | 65.4 | 43.3 | 134.5 | 20.8 | 27.6 | 65.6 | 138.5 | 84.0 |
| Nb | 2.7 | 3.3 | 2.7 | 3.8 | 4.3 | 3.8 | 8.4 | 4.5 | 1.7 | 2.1 | 4.2 | 4.2 | 4.0 | 3.7 | 4.4 | 8.7 | 2.3 | 5.1 | 9.9 | 7.4 | 7.3 |
| Mo | 1.43 | 0.59 | 0.54 | 0.59 | 0.92 | 0.66 | 1.15 | 0.42 | 0.95 | 1.75 | 0.79 | 0.85 | 1.76 | 0.95 | 0.47 | 0.59 | 0.69 | 0.75 | 1.38 | 3.14 | 0.79 |
| Cd | 0.07 | 0.06 | 0.03 | 0.09 | 0.77 | 0.08 | 0.06 | 0.07 | 0.54 | 0.49 | 0.03 | 0.04 | 0.07 | 0.03 | 0.74 | 0.03 | 0.11 | 0.12 | 0.15 | <0.02 | <0.02 |
| Sn | 0.9 | 1.5 | 1.4 | 1.0 | 1.4 | 1.0 | 1.7 | 1.3 | 0.8 | 1.0 | 1.6 | 1.4 | 1.6 | 1.4 | 1.9 | 1.8 | 1.7 | 1.3 | 1.0 | 2.6 | 1.4 |
| Cs | 1.27 | 1.97 | 3.01 | 0.99 | 0.42 | 1.24 | 1.72 | 0.23 | 2.57 | 2.76 | 6.06 | 0.97 | 3.25 | 1.98 | 5.69 | 3.86 | 2.05 | 2.07 | 0.53 | 1.07 | 0.86 |
| Ba | 280 | 430 | 410 | 210 | 250 | 220 | 380 | 140 | 500 | 290 | 1180 | 1390 | 210 | 720 | 470 | 1330 | 670 | 220 | 390 | 50 | 280 |
| La | 5.6 | 7.8 | 8.1 | 11.1 | 13.2 | 12.5 | 19.3 | 10.7 | 3.2 | 6.8 | 7.9 | 10.5 | 29.2 | 18.3 | 15.0 | 14.6 | 7.7 | 10.4 | 20.3 | 17.9 | 20.1 |
| Ce | 15.60 | 24.6 | 23.5 | 28.2 | 33.7 | 31.3 | 48.1 | 28.0 | 10.15 | 18.20 | 22.4 | 24.8 | 70.4 | 44.5 | 35.0 | 33.6 | 18.95 | 27.3 | 36.8 | 42.9 | 43.9 |
| Pr | 1.98 | 3.69 | 3.49 | 4.07 | 4.84 | 4.53 | 6.74 | 4.11 | 1.25 | 2.36 | 2.98 | 3.08 | 9.11 | 5.67 | 4.14 | 4.25 | 2.46 | 3.50 | 4.15 | 5.16 | 5.17 |
| Nd | 8.5 | 16.2 | 15.1 | 17.4 | 20.7 | 19.5 | 27.6 | 17.9 | 6.2 | 11.0 | 14.3 | 14.0 | 39.8 | 25.0 | 17.7 | 18.3 | 11.0 | 14.6 | 13.9 | 21.5 | 21.2 |
| Sm | 2.39 | 4.21 | 3.71 | 4.28 | 5.08 | 4.71 | 6.23 | 4.63 | 1.84 | 3.06 | 4.09 | 3.76 | 8.79 | 5.80 | 4.56 | 5.03 | 2.83 | 3.13 | 2.69 | 4.94 | 5.32 |
| Eu | 0.68 | 1.07 | 0.95 | 1.32 | 1.52 | 1.48 | 2.02 | 1.49 | 0.62 | 1.18 | 1.09 | 1.01 | 2.20 | 1.37 | 1.76 | 2.11 | 0.85 | 0.73 | 2.11 | 0.91 | 1.60 |
| Gd | 2.84 | 4.46 | 4.01 | 4.67 | 5.26 | 5.13 | 6.33 | 5.35 | 2.28 | 3.43 | 4.37 | 3.92 | 8.28 | 5.67 | 4.89 | 5.47 | 3.07 | 2.65 | 1.93 | 4.31 | 5.52 |
| Tb | 0.48 | 0.69 | 0.61 | 0.68 | 0.76 | 0.75 | 0.93 | 0.79 | 0.39 | 0.55 | 0.71 | 0.66 | 1.13 | 0.89 | 0.76 | 0.95 | 0.54 | 0.38 | 0.28 | 0.70 | 0.91 |
| Dy | 3.00 | 4.16 | 3.74 | 3.96 | 4.41 | 4.29 | 5.32 | 4.55 | 2.52 | 3.36 | 4.57 | 4.14 | 6.59 | 5.61 | 4.42 | 6.21 | 3.56 | 2.29 | 1.56 | 4.41 | 5.52 |
| Ho | 0.64 | 0.87 | 0.78 | 0.80 | 0.89 | 0.87 | 1.02 | 0.90 | 0.54 | 0.70 | 0.96 | 0.88 | 1.33 | 1.19 | 0.89 | 1.33 | 0.77 | 0.51 | 0.31 | 0.95 | 1.13 |
| Er | 1.84 | 2.44 | 2.22 | 2.17 | 2.44 | 2.33 | 2.69 | 2.37 | 1.56 | 2.08 | 2.85 | 2.64 | 3.82 | 3.50 | 2.45 | 4.05 | 2.24 | 1.73 | 0.93 | 2.97 | 3.35 |
| Tm | 0.27 | 0.34 | 0.31 | 0.30 | 0.33 | 0.32 | 0.35 | 0.30 | 0.21 | 0.29 | 0.41 | 0.37 | 0.51 | 0.48 | 0.33 | 0.57 | 0.31 | 0.28 | 0.15 | 0.44 | 0.50 |
| Yb | 1.85 | 2.30 | 2.12 | 1.96 | 2.18 | 2.13 | 2.17 | 1.92 | 1.50 | 2.01 | 2.95 | 2.67 | 3.45 | 3.34 | 2.26 | 4.13 | 2.06 | 2.09 | 1.16 | 3.22 | 3.57 |

| | | | | | | | | | | | | | | | | | | | | | | |
|---|---|---|---|---|---|---|---|---|---|---|---|---|---|---|---|---|---|---|---|---|---|---|
| Lu | 0.28 | 0.33 | 0.30 | 0.28 | 0.31 | 0.31 | 0.29 | 0.25 | 0.24 | 0.31 | 0.48 | 0.44 | 0.53 | 0.52 | 0.35 | 0.67 | 0.31 | 0.37 | 0.18 | 0.52 | 0.59 | |
| Hf | 1.9 | 2.1 | 2.0 | 3.2 | 3.5 | 3.4 | 3.9 | 2.9 | 0.6 | 1.0 | 3.3 | 3.1 | 2.0 | 2.0 | 1.3 | 4.0 | 0.6 | 0.8 | 2.7 | 4.6 | 2.5 | |
| Ta | 0.19 | 0.21 | 0.18 | 0.23 | 0.25 | 0.24 | 0.47 | 0.27 | 0.12 | 0.15 | 0.29 | 0.28 | 0.28 | 0.26 | 0.32 | 0.65 | 0.17 | 0.34 | 0.89 | 0.50 | 0.64 | |
| W | 0.6 | 0.4 | 0.3 | 0.3 | 0.4 | 0.3 | 0.4 | 0.3 | 2.1 | 0.8 | 1.0 | 0.8 | 1.7 | 4.1 | 1.8 | 1.6 | 0.8 | 2.7 | 0.6 | 1.5 | 1.1 | |
| Pb | 5.7 | 6.0 | 2.5 | 5.3 | 19.0 | 5.1 | 6.5 | 8.2 | 8.1 | 5.1 | 4.1 | 3.9 | 7.4 | 5.5 | 34.7 | 6.4 | 8.8 | 17.0 | 23.8 | 3.6 | 4.2 | |
| Bi | 0.03 | 0.22 | 0.11 | 0.02 | 0.03 | 0.02 | 0.04 | 0.02 | 0.06 | 0.04 | 0.04 | 0.06 | 0.07 | 0.04 | 0.05 | 0.05 | 0.08 | 0.15 | 0.03 | 0.03 | 0.05 | |
| Th | 2.0 | 3.3 | 3.1 | 1.7 | 2.1 | 2.0 | 1.3 | 1.2 | 0.8 | 1.4 | 3.0 | 2.8 | 3.1 | 2.5 | 2.7 | 7.1 | 1.4 | 3.4 | 14.8 | 9.8 | 9.2 | |
| U | 0.8 | 1.0 | 1.0 | 0.7 | 0.8 | 0.8 | 0.5 | 0.5 | 0.4 | 0.5 | 1.2 | 1.0 | 1.1 | 0.9 | 1.1 | 1.9 | 0.5 | 0.6 | 5.9 | 2.6 | 1.9 | |

$SiO_2$ of 46.98–51.99 wt.%, MgO of 3.36–6.38 wt.%, $Al_2O_3$ of 15.59–18.56 wt.% and $Fe_2O_3^T$ of 8.8–10.74 wt.%, with Mg# of 47.1–60.7. Their Cr and Ni contents are of 5–168 ppm and 4.6–113 ppm, respectively. In the chondrite-normalized REE diagram (Fig. 6a), the basalt and diabase have a slight enrichment of light rare earth elements (LREEs) with $(La/Yb)_N = 1.53–6.38$, with or without slight Eu anomalies ($\delta Eu = 0.89–1.11$). In the primitive mantle-normalized multi-element diagram (Fig. 6b), the rocks are depleted in high field strength elements (HFSEs; e.g., Nb, Ta, Zr, Hf, P and Ti) and enriched in large ion lithophile elements (LILEs; e.g., Rb, Ba, K, Pb and Sr). These features are consistent with those of modern back-arc basin (BAB) basalts, e.g., basalts from the Okinawa Trough (Fig. 6) (Shinjo et al., 1999).

Andesite has $SiO_2$ of 56.87–60.42 wt.%, MgO of 1.48–3.18 wt.%, $Al_2O_3$ of 14.62–16.78 wt.% and $Fe_2O_3^T$ of 3.29–11.74 wt.%, with Mg# of 36.1–55.8, whereas the andesitic tuff and diorite contain $SiO_2$ (52.98–61.83 wt.%), MgO (1.88–4.53 wt.%), $Al_2O_3$ (16.32–18.03 wt.%) and $Fe_2O_3^T$ (5.02–13.03 wt.%), with Mg# (36.8–55.0). Compared with the andesite, andesitic tuff and diorite, the rhyolite contains higher $SiO_2$ (66.75–70.87 wt.%), but lower $Al_2O_3$ (9.91–14.60 wt.%), $Fe_2O_3^T$ (1.53–7.03 wt.%) and MgO (0.43–3.95 wt.%). In the chondrite-normalized REE diagram (Fig. 6c, e, g), all the Shaquanzi intermediate to felsic rocks show enrichment of LREE and depletion of HREE, with $(La/Yb)_N = 1.92–6.07$ (except for one rhyolite, whose $(La/Yb)_N = 12.55$). Most of the Shaquanzi intermediate to felsic rocks have negative Eu anomalies ($\delta Eu = 0.59–0.89$), suggesting plagioclase fractionation. The REE patterns of Shaquanzi intermediate to felsic rocks mimic those of modern back-arc basin rhyolites (BABR) from the Okinawa Trough (Fig. 6) (Shinjo and Kato, 2000). In the primitive mantle-normalized multi-element diagram (Fig. 6b, d, f), the andesite, andesitic tuff and diorite are LILEs enriched, and HFSEs depleted, similar to the Shaquanzi basalt and diabase porphyrite. The rhyolite is similar to the Okinawa Trough BAB rhyolite (Shinjo and Kato, 2000).

### 5.3. Whole-rock Sr-Nd-Pb isotopes

The Sr-Nd isotopic calculations for the volcanic rocks were based on the age of 315 Ma, and diorite on 298 Ma. Our results show that the basalt, andesite, rhyolite and diorite have different isotopic compositions (Table 3; Fig. 7a). The basalt has initial $^{87}Sr/^{86}Sr$ ratios (Isr) of 0.7043 to 0.7046, $\varepsilon_{Nd}(t)$ values of +3.11 to +5.61, and single-stage depleted mantle Nd model ages ($T_{DM1}$) of 0.68–0.94 Ga. The andesite has initial $^{87}Sr/^{86}Sr$ ratios (Isr) of 0.7045 to 0.7049, $\varepsilon_{Nd}(t)$ values of +2.12 to +5.56, and two-stage depleted mantle Nd model ages ($T_{DM2}$) of 0.70–0.91 Ga. In contrast, the rhyolite has lower initial $^{87}Sr/^{86}Sr$ ratios (Isr = 0.7039–0.7040), lower $\varepsilon_{Nd}(t)$ values (−0.21 and + 1.49), and older two-stage depleted mantle Nd model ages ($T_{DM2}$ = 0.96–1.1 Ga) (calculated after Huang et al., 2013a). Compared with the volcanic rocks, the diorite show higher initial $^{87}Sr/^{86}Sr$ ratios (Isr = 0.7048–0.7051), distinctly positive $\varepsilon_{Nd}(t)$ values (+4.17 to +4.35), and two-stage depleted mantle Nd model ages ($T_{DM2}$) of 0.71–0.73 Ga. As shown in Fig. 7a, the Shaquanzi volcanic rocks and diorites have similar Sr-Nd isotopic compositions to those of the Okinawa Trough BAB (Shinjo et al., 1999; Shinjo and Kato, 2000).

The Shaquanzi diorite has $^{206}Pb/^{204}Pb$ = 18.45–19.33 (average = 18.80), $^{207}Pb/^{204}Pb$ = 15.55–15.60 (average = 15.57), and $^{208}Pb/^{204}Pb$ = 38.32–39.10 (average = 38.62), similar to the Ryukyu Arc and Okinawa Trough BAB (Fig. 7b–d) (Hoang and Uto, 2006; Zeng et al., 2010). The diorite plots in the mantle array between depleted mantle (DM) and bulk silicate earth (BSE) with restricted ranges (Fig. 7b), indicating that their sources were uniformly depleted in terms of isotopic compositions. This conclusion

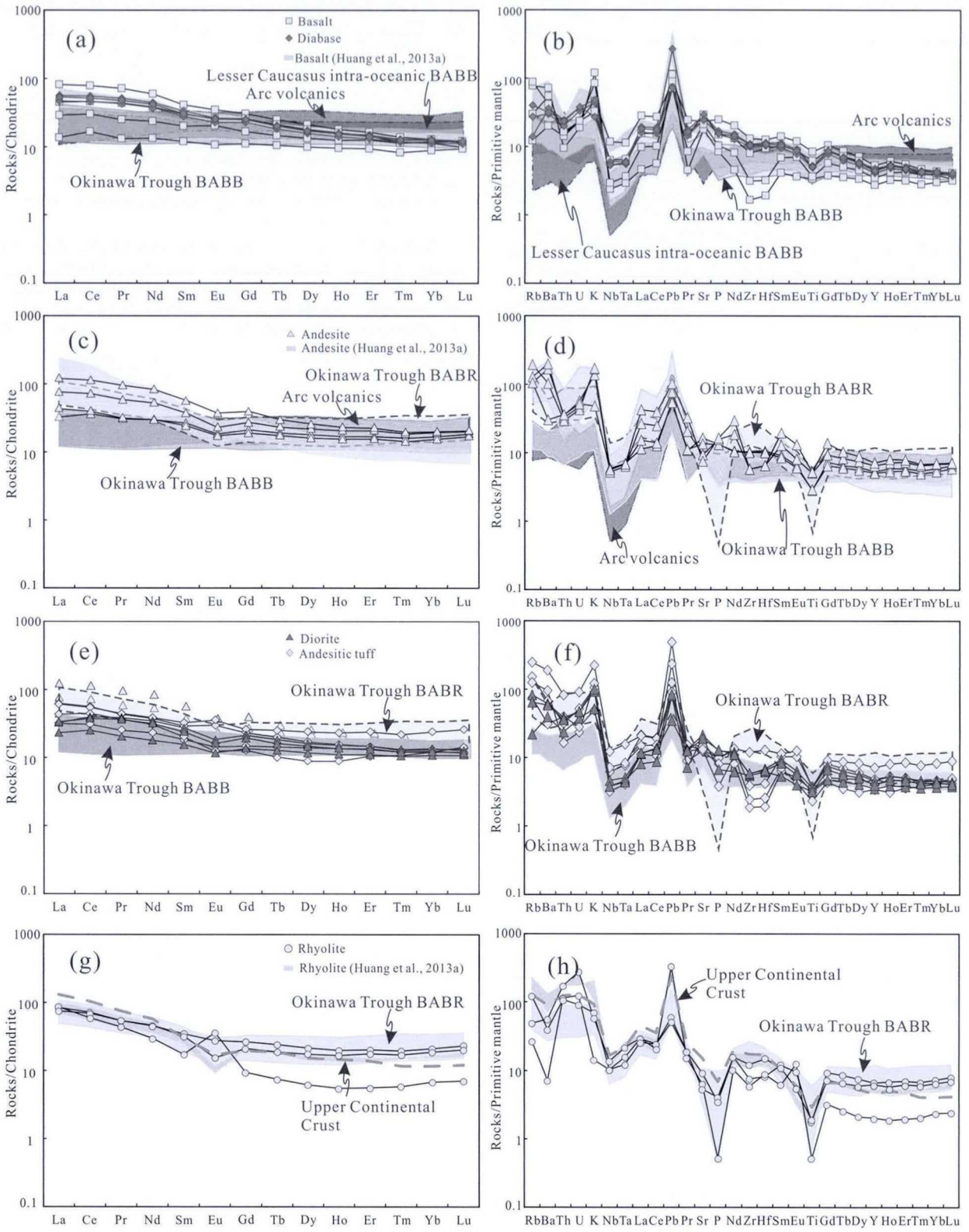


**Figure 6.** Chondrite-normalized REE diagram and primitive mantle-normalized multi-element spider diagram for the Shaquanzi Formation. Compositions for the average primitive mantle and chondrite data are from Sun and McDonough (1989). Data of the Okinawa Trough BABB, Lesser Caucasus intra-oceanic BABB (the blue dash line filled with pink in Fig. 6a and b), Okinawa Trough BABR (the enclosed blue dash line in Fig. 6d–h) and arc volcanics (the red dash line filled with green in Fig. 6c–h) are from Shinjo et al. (1999), Shinjo and Kato (2000), Luhr and Haldar (2006), Rolland et al. (2009), respectively. Upper Continental Crust data are from Rudnick and Gao (2003).

**Table 3**
Sr–Nd isotopic data for the volcanic rocks and diorite from the Shaquanzi area.

| Sample | Rock | Age (Ma) | $^{87}Rb/^{86}Sr$ | $^{87}Sr/^{86}Sr$ | 2σ | $I_{Sr}$ | $^{147}Sm/^{144}Nd$ | $^{143}Nd/^{144}Nd$ | 2σ | $\varepsilon_{Nd}(t)$ | $T_{DM1}$ | $T_{DM2}$ | $f_{Sm/Nd}$ | $^{206}Pb_i/^{204}Pb$ | $^{207}Pb_i/^{204}Pb$ | $^{208}Pb_i/^{204}Pb$ | $^{206}Pb_i/^{204}Pb_i$ | $^{207}Pb_i/^{204}Pb_i$ | $^{208}Pb_i/^{204}Pb_i$ |
|---|---|---|---|---|---|---|---|---|---|---|---|---|---|---|---|---|---|---|---|
| Diorite | ZK2-12 | 298.5 | 0.097874 | 0.705238 | 0.000007 | 0.7048 | 0.171258 | 0.512802 | 0.000005 | 4.17 | 1.26 | 0.73 | −0.13 | 18.447 | 15.550 | 38.316 | 17.963 | 15.524 | 37.934 |
| | ZK5-1 | 298.5 | 0.338151 | 0.706187 | 0.000006 | 0.7048 | 0.158284 | 0.512783 | 0.000005 | 4.29 | 1.01 | 0.72 | −0.20 | 18.631 | 15.562 | 38.453 | 18.054 | 15.531 | 37.851 |
| | ZK5-6 | 298.5 | 0.294383 | 0.706346 | 0.000007 | 0.7051 | 0.149647 | 0.512769 | 0.000005 | 4.35 | 0.91 | 0.71 | −0.24 | 19.332 | 15.600 | 39.095 | 17.920 | 15.527 | 37.711 |
| Basalt* | SQZ0901 | 314.7 | 0.142594 | 0.705157 | 0.000021 | 0.7045 | 0.138789 | 0.512806 | 0.000003 | 5.61 | 0.70 | 0.62 | −0.29 | | | | | | |
| | SQZ0907 | 314.7 | 0.204075 | 0.705177 | 0.000014 | 0.7043 | 0.136433 | 0.512673 | 0.000004 | 3.11 | 0.94 | 0.82 | −0.31 | | | | | | |
| | SQZ0910 | 314.7 | 0.353690 | 0.706145 | 0.000007 | 0.7046 | 0.132816 | 0.512791 | 0.000003 | 5.56 | 0.68 | 0.62 | −0.32 | | | | | | |
| Andesite* | SQZ0912 | 314.7 | 0.283003 | 0.706147 | 0.000008 | 0.7049 | 0.125470 | 0.512730 | 0.000003 | 4.66 | 0.73 | 0.70 | −0.36 | | | | | | |
| | SQZ0913 | 314.7 | 1.089460 | 0.709359 | 0.000011 | 0.7045 | 0.139281 | 0.512668 | 0.000004 | 2.90 | 0.99 | 0.84 | −0.29 | | | | | | |
| | SQZ0914 | 314.7 | 1.209990 | 0.709880 | 0.000007 | 0.7045 | 0.104676 | 0.512557 | 0.000003 | 2.12 | 0.83 | 0.91 | −0.47 | | | | | | |
| Rhyolite* | SQZ0904 | 314.7 | 1.740883 | 0.711757 | 0.000011 | 0.7040 | 0.125719 | 0.512481 | 0.000002 | −0.21 | 1.16 | 1.10 | −0.36 | | | | | | |
| | SQZ0905 | 314.7 | 2.312018 | 0.714355 | 0.000010 | 0.7040 | 0.136334 | 0.512590 | 0.000003 | 1.49 | 1.11 | 0.96 | −0.31 | | | | | | |

Samples with "*" are from Huang et al. (2013a).

is also supported by the $^{206}Pb/^{204}Pb$, $^{207}Pb/^{204}Pb$ and $^{208}Pb/^{204}Pb$ isotopic system, of which the samples lie along or near the mantle evolution curve (Fig. 7c and d).

### 5.4. In-situ zircon Hf isotopic compositions

Lu-Hf isotope spot analyses were performed on eight dated zircons from the andesite (Y-12). The results indicate high $^{176}Lu/^{177}Hf$ ratios of 0.000790–0.001652 and relatively wide range of $^{176}Hf/^{177}Hf = 0.282573–0.282951$ (Table 4; Fig. 8). The calculated $\varepsilon_{Hf}(t) = -0.12$ to $+13.04$, and the corresponding two-stage Hf model ages ($T_{DM2}$) = 499–1341 Ma. Lu-Hf isotopic analyses were obtained on twelve dated zircons from the andesitic tuff sample (ZK1-112). The results also indicate high $^{176}Lu/^{177}Hf$ = 0.001087–0.002955 and relatively wide range of $^{176}Hf/^{177}Hf$ = 0.282749–0.282888 (Table 4; Fig. 8). The calculated $\varepsilon_{Hf}(t)$ values = 5.80–10.69. The corresponding two-stage Hf model ages ($T_{DM2}$) = 641–957 Ma. All the data points plot between the depleted mantle and CHUR line in the $\varepsilon_{Hf}(t)$ vs. $t$ diagram (Fig. 8), which are similar to those of zircon grains from Phanerozoic igneous rocks in the CAOB (Xiao et al., 2004; Chen et al., 2009; Qian et al., 2014).

## 6. Discussion

### 6.1. Ages of magmatism at Shaquanzi

#### 6.1.1. Shaquanzi Formation volcanic rocks

The Shaquanzi Formation is dominated by mafic-intermediate volcanic lava, pyroclastic rocks and minor felsic volcanic rocks and carbonates (Chen et al., 2003; Huang et al., 2013a, 2014a). The Late Carboniferous marine fusulinids fossils (e.g., *Schubertella* sp. and *Ozawuainella* sp.) recovered in limestone at Lubaishan (Zhang et al., 2012) and adjacent regions (Cai, 1999; Chen et al., 2003) show that the Shaquanzi Formation was formed in the Late Carboniferous. In this study, we present the first precise radiometric ages for the Shaquanzi Formation volcanic rocks.

Zircon U-Pb dating of the andesite (314.7 ± 3.0 Ma) and andesitic tuff (305.3 ± 3.5 Ma) suggests that these rocks were formed in the Late Carboniferous, consistent with the fusulinids (Cai, 1999; Zhang et al., 2012).

#### 6.1.2. Shaquanzi diorite

The diorite shows intrusive relationship with the volcanic strata of the Shaquanzi Formation. Our new zircon U-Pb dating has yielded earliest Permian age (298.5 ± 5.1 Ma) for the diorite, similar to the mineralization age of the Shaquanzi Fe–(Cu) deposit (303 ± 12 Ma for the magnetite and 297 ± 7 Ma for the pyrite by Re-Os dating) (Huang et al., 2013b, 2014b). Although their genetic links remain unclear, their similar age possibly indicates an important magmatic event in the Yamansu belt during the Late Carboniferous to the earliest Permian, as also supported by the study of the granitoids (ages ranging 320–252 Ma) in the Jueluotage area (Zhou et al., 2010).

### 6.2. Petrogenesis of the volcanic rocks and diorite

Due to the alteration of rocks around the Shaquanzi Fe–(Cu) deposit, we focus mainly on immobile elements (e.g., Al, Th, REEs and HFSEs) and transition elements (e.g., Sc, V, Ni and Cu) (Winchester and Floyd, 1976, 1977; Condie, 2005; Said and Kerrich, 2009; Chen et al., 2013; Li et al., 2013) in our petrogenetic discussion.

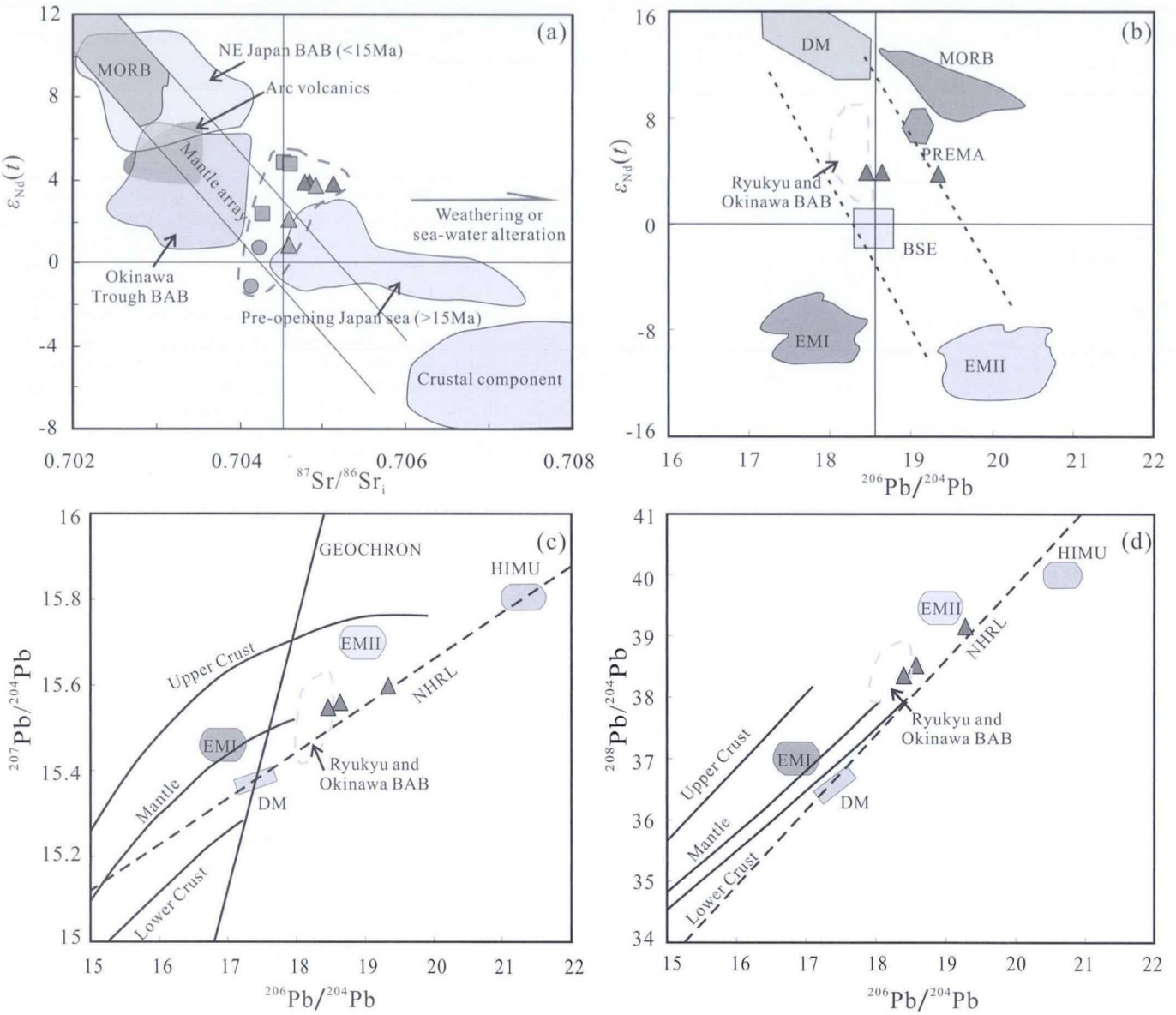


**Figure 7.** Discrimination diagrams of the radiogenic isotopes for the Shaquanzi Formation igneous rocks: (a) Initial $\varepsilon_{Nd}(t)$ vs. $^{87}Sr/^{86}Sr(t)$ diagram ($t$ = 315 Ma for the volcanic rocks, $t$ = 298.5 Ma for the diorites). Fields of the Early and Middle–Late Miocene northeast Japan BAB, Okinawa Trough BAB and arc volcanics are from Meng et al. (1999), Shinjo et al. (1999), Huang et al. (2006), Luhr and Haldar (2006), Shuto et al. (2006), Zeng et al. (2010). (b) $\varepsilon_{Nd}(t)$ vs. $^{206}Pb/^{204}Pb$ diagram after Zindler and Hart (1986); (c) $^{207}Pb/^{204}Pb$ vs. $^{206}Pb/^{204}Pb$ diagram after Li et al. (2001); and (d) $^{208}Pb/^{204}Pb$ vs. $^{206}Pb/^{204}Pb$ diagram after Li et al. (2001). NHRL = Northern Hemisphere reference line (Hart, 1984); BSE = Bulk silicate earth (Zindler and Hart, 1986); DM = Depleted mantle (Zindler and Hart, 1986); MORB = Mid-oceanic ridge basalts (Zindler and Hart, 1986); EM I = Enriched mantle with low $^{87}Sr/^{86}Sr$ (Zindler and Hart, 1986); EM II = Enriched mantle with high $^{87}Sr/^{86}Sr$ (Zindler and Hart, 1986); HIMU = A high U/Pb mantle component (Zindler and Hart, 1986). Fields of the Ryukyu and Okinawa BAB are from Hoang and Uto (2006) and Zeng et al. (2010).

*6.2.1. Basalt and diabase porphyrite*

As shown in Fig. 6b, the basalt and diabase porphyrite are enriched in LILEs and depleted in HFSEs, which can be caused either by subduction or crustal contamination (Shinjo et al., 1999; Rudnick and Gao, 2003; Wang et al., 2013a). Nevertheless, rocks formed by crustal contamination generally do not show distinct negative Zr-Hf anomalies because of the abundances of Zr and Hf in the crust (Qian et al., 2014). Although two samples display distinctive negative Zr-Hf anomalies (Fig. 6b), the crustal contamination-sensitive trace elements/element ratios (e.g., Th, Zr, $\varepsilon_{Nd}(t)$, Nb/La, $(La/Sm)_N$) do not show any correlation with MgO to prove the contamination (Wang et al., 2013a) (Fig. 9a and b). Th and Nb contents in the parental magmas change with crustal contamination and/or incorporation of subducted sediments/metasomatic fluids, thus the Th/Yb vs. Nb/Yb diagram can reveal the relative input of crustal materials vs. subduction-related inputs into the magmatic system (Pearce, 2008; Li et al., 2013). In this study, the basalt and diabase porphyrite data points fall above the mantle array and close to the fields of the BABB from the Okinawa Trough, Mariana Trough and the East Scotia Ridge, but far from the average upper continental crust (Fig. 10) (Li et al., 2013). Consequently, we conclude that the Shaquanzi basaltic magma might have originated from a subduction-related source without crustal contamination.

Primary basaltic magma originated from partial melting of mantle peridotite should have Mg# in the range of 68.0–75.0 (Green, 1973; Hanson and Langmuir, 1978), and would be characterized by 250–300 ppm Ni, 500–600 ppm Cr and 27–80 ppm Co (Frey et al., 1978; Perfit et al., 1980; Wilkinson and Le Maitre, 1987).

**Table 4**
In situ zircon Hf isotopic data for the volcanic rocks from the Shaquanzi area.

| Sample | $t$ (Ma) | $^{176}Yb/^{177}Hf$ | $^{176}Lu/^{177}Hf$ | $^{176}Hf/^{177}Hf$ | $2\sigma$ | $\varepsilon_{Hf}(0)$ | $\varepsilon_{Hf}(t)$ | $2\sigma$ | $T_{DM1}$ | $T_{DM2}$ | $f_{Lu/Hf}$ |
|---|---|---|---|---|---|---|---|---|---|---|---|
| Y-12-1 | 321 | 0.021228 | 0.000890 | 0.282679 | 0.000010 | −3.29 | 3.6 | 0.4 | 0.81 | 1.10 | −0.97 |
| Y-12-2 | 323 | 0.020102 | 0.000790 | 0.282573 | 0.000015 | −7.05 | −0.1 | 0.5 | 0.96 | 1.34 | −0.98 |
| Y-12-4 | 322 | 0.036743 | 0.001523 | 0.282877 | 0.000012 | 3.70 | 10.5 | 0.4 | 0.54 | 0.66 | −0.95 |
| Y-12-6 | 393 | 0.039177 | 0.001609 | 0.282908 | 0.000010 | 4.80 | 13.0 | 0.3 | 0.50 | 0.55 | −0.95 |
| Y-12-8 | 313 | 0.023412 | 0.000974 | 0.282681 | 0.000017 | −3.23 | 3.4 | 0.6 | 0.81 | 1.11 | −0.97 |
| Y-12-11 | 319 | 0.039773 | 0.001652 | 0.282951 | 0.000010 | 6.34 | 13.0 | 0.3 | 0.43 | 0.50 | −0.95 |
| Y-12-16 | 315 | 0.025247 | 0.001246 | 0.282779 | 0.000014 | 0.25 | 6.9 | 0.5 | 0.67 | 0.89 | −0.96 |
| Y-12-18 | 321 | 0.034488 | 0.001408 | 0.282941 | 0.000019 | 5.98 | 12.7 | 0.7 | 0.45 | 0.52 | −0.96 |
| Zk1-112-1 | 311 | 0.062725 | 0.002341 | 0.282853 | 0.000009 | 2.86 | 9.2 | 0.3 | 0.59 | 0.74 | −0.93 |
| Zk1-112-2 | 309 | 0.035353 | 0.001477 | 0.282824 | 0.000013 | 1.84 | 8.3 | 0.5 | 0.61 | 0.79 | −0.96 |
| Zk1-112-4 | 310 | 0.029821 | 0.001199 | 0.282888 | 0.000010 | 4.11 | 10.7 | 0.4 | 0.52 | 0.64 | −0.96 |
| Zk1-112-7 | 314 | 0.035873 | 0.001458 | 0.282749 | 0.000015 | −0.81 | 5.8 | 0.5 | 0.72 | 0.96 | −0.96 |
| Zk1-112-9 | 313 | 0.035933 | 0.001480 | 0.282850 | 0.000011 | 2.77 | 9.4 | 0.4 | 0.58 | 0.73 | −0.96 |
| Zk1-112-11 | 298 | 0.026465 | 0.001087 | 0.282854 | 0.000012 | 2.92 | 9.3 | 0.4 | 0.56 | 0.72 | −0.97 |
| Zk1-112-13 | 291 | 0.038686 | 0.001574 | 0.282801 | 0.000014 | 1.03 | 7.1 | 0.5 | 0.65 | 0.85 | −0.95 |
| Zk1-112-14 | 307 | 0.033696 | 0.001435 | 0.282824 | 0.000014 | 1.83 | 8.3 | 0.5 | 0.61 | 0.79 | −0.96 |
| Zk1-112-15 | 305 | 0.043656 | 0.001769 | 0.282807 | 0.000011 | 1.25 | 7.6 | 0.4 | 0.64 | 0.83 | −0.95 |
| Zk1-112-21 | 304 | 0.075977 | 0.002955 | 0.282786 | 0.000012 | 0.50 | 6.6 | 0.4 | 0.70 | 0.90 | −0.91 |
| Zk1-112-25 | 297 | 0.029854 | 0.001236 | 0.282840 | 0.000011 | 2.41 | 8.7 | 0.4 | 0.59 | 0.76 | −0.96 |
| Zk1-112-29 | 298 | 0.034344 | 0.001401 | 0.282880 | 0.000017 | 3.81 | 10.1 | 0.6 | 0.53 | 0.67 | −0.96 |

However, the basalt and diabase from the Shaquanzi Formation have low MgO (3.36–6.38 wt.%), with Mg# = 47.1–60.7, together with low Cr (5–168 ppm), Co (16.2–36.5 ppm) and Ni (4.6–113.0 ppm), suggesting their derivation from relatively evolved melts rather than a primary mantle-derived magmatic source. The decrease of $TiO_2$ and $P_2O_5$ with increasing $SiO_2$ suggests the fractional crystallization of Fe-Ti oxides and apatite (Appendix 1). Cr and Ni have positive relationship with MgO (Fig. 9c and d), indicating the fractionation of olivine and clinopyroxene. Plagioclase fractionation may not have played important role, as suggested by the slight Eu anomaly and lack of negative Sr anomaly for the basalt and diabase (Fig. 6).

As discussed above, the formation of basalt and diabase porphyrite was most likely to be subduction-related and addition of subducted materials into the melt leads to Th/Nb variations in the rocks (Pearce, 2008; Li et al., 2013). Pearce (2008) used the concentration in subducted sediment, averaged from different subduction systems (Plank and Langmuir, 1998) to model the Th-Nb variations in volcanic rocks with the amount of subduction component input into the mantle wedge. According to this model,

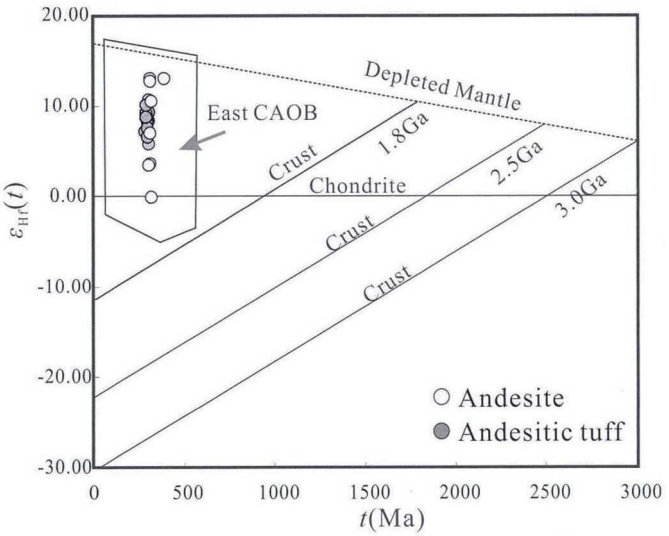


**Figure 8.** $\varepsilon_{Hf}(t)$ vs. $t$ diagram of the Shaquanzi Formation volcanic rocks. The data source of East CAOB come from Qian et al. (2014).

the Shaquanzi basaltic magma was generated from moderately depleted mantle source, with only 3–5% subducted material components (Fig. 10).

In addition, the Shaquanzi mafic rocks show selective enrichment of LILEs and LREEs and positive Pb and Sr anomalies in the primitive mantle-normalized multi-element diagram (Fig. 6a and b). The primitive mantle is depleted in LILEs, LREEs, Pb and Sr, and the Shaquanzi mafic rocks are different from OIB as revealed in Fig. 10. Meanwhile, the geochemical data shows that the crustal contamination did not play an important role in the formation of the Shaquanzi mafic rocks. Their mantle source could have been metasomatized before partial melting (Wang et al., 2013a). Hydrous melts and slab-derived fluids are generally thought to be the two main metasomatic media in subduction zones. Hydrous melts transport both water-soluble and water-insoluble materials, whereas slab-derived fluids generally transport water-soluble materials (Zheng, 2012). In subduction zone, the Ba/La fractionation can only be reasonably achieved by elemental mobility in hydrous fluids, while Th and LREE are more immobile in fluids but mobile in melts than HREE and LILE (Woodhead et al., 2001). Therefore, elements such as Ba/La and Th/HREE can be considered as useful tracers of sediment inputs or fluid contributions (Woodhead et al., 2001; Fig. 11). Our mafic rock samples are characterized by variable Ba/La but uniform Th/Yb (Fig. 11), indicating that the mantle source may be previously enriched by slab-derived fluids rather than hydrous melt. Meanwhile, the basalt has relatively high $\varepsilon_{Nd}(t)$ values (3.11–5.61) and low initial $^{87}Sr/^{86}Sr$ ratios (0.7043–0.7046), suggesting that it was derived from the depleted mantle. The decoupling of trace element and the isotope characteristics, coupled with the enrichment of the depleted mantle source, reveal that the mantle source was metasomatized before generating the Shaquanzi basalt and diabase porphyrite.

In summary, the basaltic magma might have been derived from the depleted mantle metasomatized by subduction-related fluids with minor (3–5%) subduction material input.

### 6.2.2. Andesite

Two major petrogenetic models have been proposed for the origin of intermediate-felsic magmas in subduction zones: (1) extensive fractional crystallization of mantle-derived basaltic magma accompanied with crustal contamination (Bacon and Druitt, 1988; Pin and Paquette, 1997; Bonin, 2004; Kang et al., 2014); and (2) ensialic continental crustal anatexis caused by

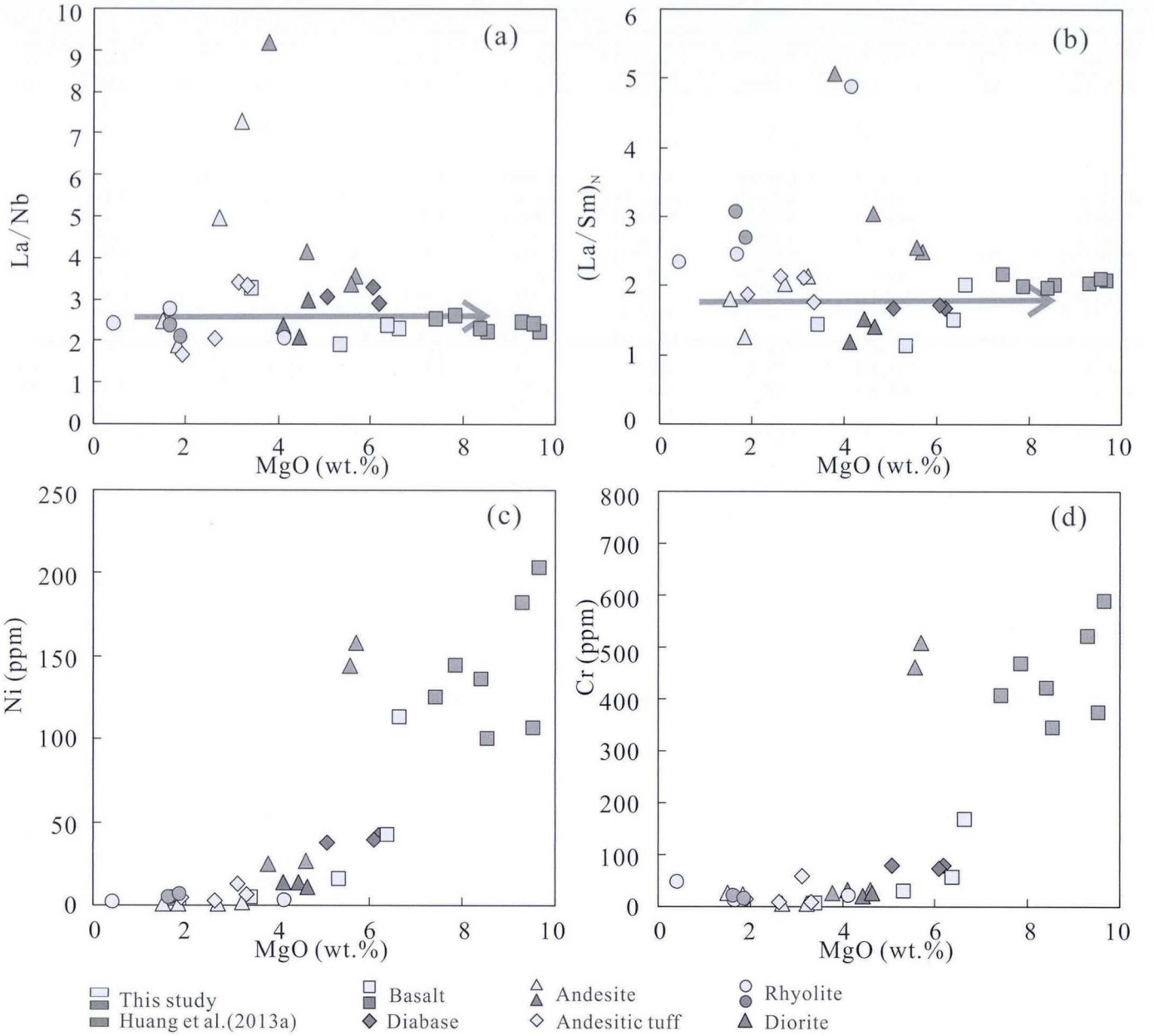


**Figure 9.** (a) La/Nb, (b) $(La/Sm)_N$, (c) Ni and (d) Cr vs. MgO diagrams of the Shaquanzi Formation igneous rocks. The normalized data of $(La/Sm)_N$ ratio are from Chondrite data normalizing (Sun and McDonough, 1989).

mantle derived mafic magmas (Roberts and Clemens, 1993; Guffanti et al., 1996; Zhu et al., 2007, 2012), whose intermediate-felsic products may display enrichments in Al, Th, LREEs and negative $\varepsilon_{Nd}(t)$ values, distinctly different from the associated mafic rocks (Zhu et al., 2007). Only high degree of fractional crystallization (over 90%) of basaltic magma can produce the silicic melts (Wilson, 1993), the first model is thus used to account for the generation of small scale felsic melts (Shinjo and Kato, 2000; Riley et al., 2001; Ayalew and Yirgu, 2003). In contrast, the second model can produce abundant felsic magma, and is widely accepted as an effective mechanism for generating felsic-dominated magmatism (Guffanti et al., 1996; Zhu et al., 2012; Chen et al., 2014).

The Shaquanzi Formation is dominantly intermediate-mafic rocks, with minor felsic rocks (Huang et al., 2013a) and the $\varepsilon_{Nd}(t)$ values of the andesite and rhyolite range from 2.12 to 4.66 and −0.21 to 1.49, respectively, resembling those of the Shaquanzi mafic rocks (3.11–5.61) and suggesting that continental crustal anatexis was not involved in the formation of Shaquanzi intermediate-felsic rocks. This is further supported by the REE and primitive mantle-normalized multi-element patterns of the andesite (Fig. 6) and nearly all data points fall along a trend of the basalt in the Harker diagram (Appendix 1). The andesites are more depleted in P and Ti than the basalts, indicative of apatite and Fe-Ti oxides fractionation of the andesitic magma. The more negative Eu and Sr anomalies in the andesite suggest that plagioclase fractionation was more significant in the evolution of andesitic magma than in its basalt counterpart. However, MgO does not show distinctive linear relation with Ni and Cr (Fig. 9c and d), suggesting olivine and clinopyroxene fractionation was insignificant. Meanwhile, in the binary diagrams between MgO and the contamination-sensitive trace element/element ratios (e.g. Th, Nb/La, $(La/Sm)_N$), a few andesite data points show extraordinary high

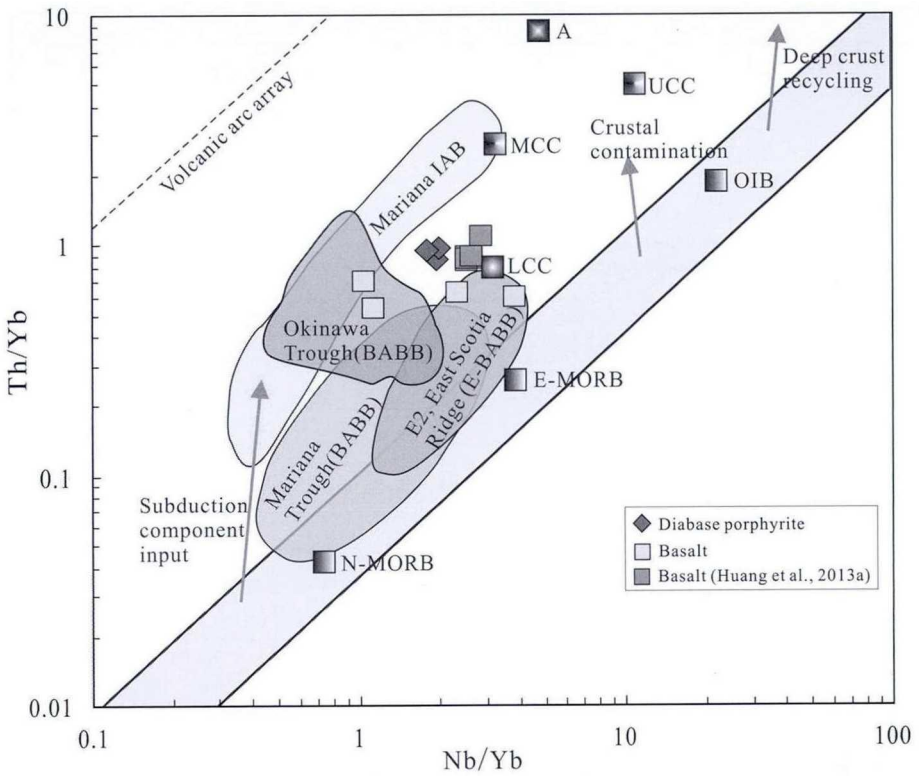


**Figure 10.** Th/Yb vs. Nb/Yb diagram discriminating rocks enriched by inputs from subduction, crustal contamination, and deep crustal recycling (modified after Pearce, 2008). Achaean (A) crust data are from Rudnick and Fountain (1995); Mariana Trough BABB and Mariana IAB data are from Pearce et al. (2005); Segment E2, East Scotia Ridge E-BABB data are from Leat et al. (2000); Okinawa Trough BABB data are from Shinjo et al. (1999); LCC, MCC, and UCC are from Rudnick and Gao (2003). Vector "C" shows the crustal contamination trend and vector "W" indicates the mantle wedge melting trend.

La/Nb and $(La/Sm)_N$ values (Fig. 9a and b), indicating certain degree of crustal contamination. This is consistent with the $\varepsilon_{Hf}(t)$ values (−0.12 to 13.04) and the two-stage Hf model ages ($T_{DM2}$ = 499–1341 Ma), which is older than formation age of the andesite (Table 4, Fig. 8).

### 6.2.3. Diorite and andesitic tuff

Andesitic tuff and diorite at Shaquanzi have similar emplacement ages within error (305.3 ± 3.5 Ma and 298.5 ± 5.1 Ma, respectively) (Fig. 4), together with similar major (Appendix 1), trace and REE patterns (Fig. 6e and f). The $\varepsilon_{Hf}(t)$ values of the andesitic tuffs range from +5.8 to +10.7, indicating a mantle source (Tables 3 and 4). Pb isotope compositions of the diorites lie along or near the mantle evolution curve (Fig. 7), consistent with the Sr-Nd isotopes, also suggestive of a depleted mantle origin. Moreover, Sr-Nd isotopes of the diorite are comparable to the basalt but different from the andesite and rhyolite (Fig. 7). Consequently, the andesitic tuffs and diorite could have been derived from the same source as the Shaquanzi Formation volcanic rocks and probably represent the pulses of mafic magmatism. The diorites also show some affinities with volcanic arc in the tectonic discrimination diagrams of granite (Fig. 12a and b).

### 6.2.4. Rhyolite

As discussed above, the intermediate-felsic rocks of the Shaquanzi Formation are probably the fractional crystallization products of basaltic magma. In the Harker diagram (Appendix 1), most andesite data points fall in between the basalt and rhyolite fields and show a quasi-trend with the basalt, suggesting that the andesite may be co-magmatic. Compared with the andesite, the rhyolite has more negative Sr anomalies and is more depleted in P and Ti, indicating the existence of fewer apatite and Fe-Ti oxides in the residue magma and significant plagioclase fractionation than the andesites during the magma evolution. In addition, the higher Zr and Hf contents and lower $\varepsilon_{Nd}(t)$ values of the rhyolite may suggest a more significant involvement of crustal materials in their genesis (Figs. 6g and h, and 7a).

In summary, we suggest that the Shaquanzi andesites and rhyolite were likely to be derived from similar source as the basalts. The rhyolite was possibly derived from basaltic magma through andesite via fractional crystallization with certain degree of crust contamination. The andesitic tuffs and diorite have the same source as the Shaquanzi Formation volcanic rocks and probably represent the pulses of mafic magmatism.

## 6.3. Tectonic setting

Our new geochemical data indicate that the Shaquanzi magmatic rocks were formed in a supra-subduction zone. Back-arc basaltic rocks have transitional geochemical composition between typical MORB and island arc basalt (IAB) (Pearce and Stern, 2006). On the ternary tectonic discrimination diagrams (Ti/50–50 × Sm–V and 2 × Nb–Zr/4–Y) (Fig. 13), the Shaquanzi Formation mafic rocks fall into the MORB–IAB transitional fields (Fig. 13a and b) (Saunders and Tarney, 1984; Pearce and Stern, 2006). Moreover, island arc mafic rocks are more oxidized than mafic rocks from the other tectonic settings (Kelley and Cottrell, 2012), which results in their high V contents and low Ti/V ratios (Shervais, 1982). The Shaquanzi Formation mafic rocks have high Ti/V but low V relative to typical IAB and fall into the field of the

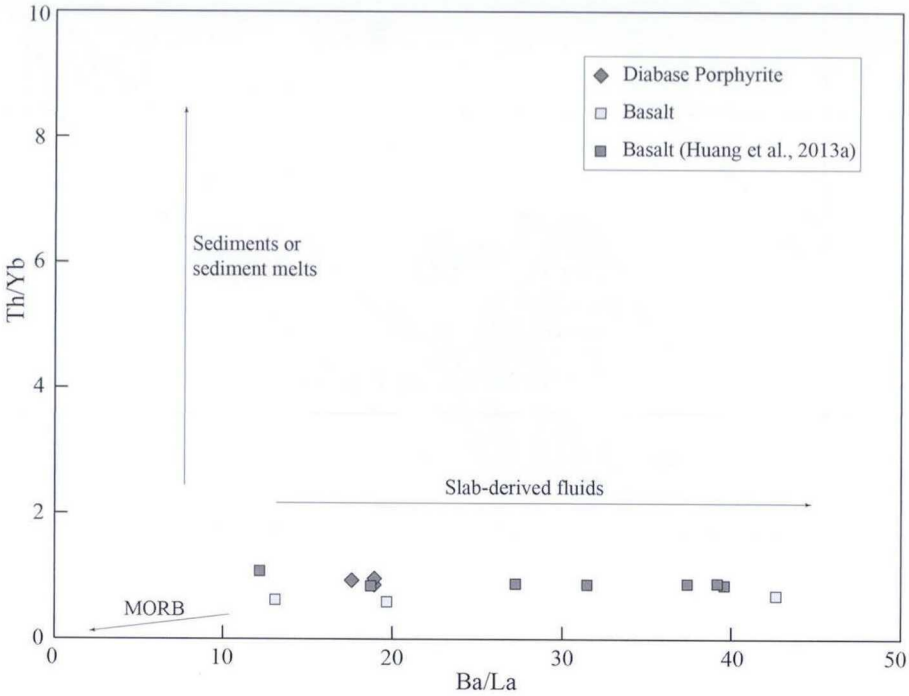


**Figure 11.** Ba/La vs. Th/Yb diagram (modified after Woodhead et al., 2001).

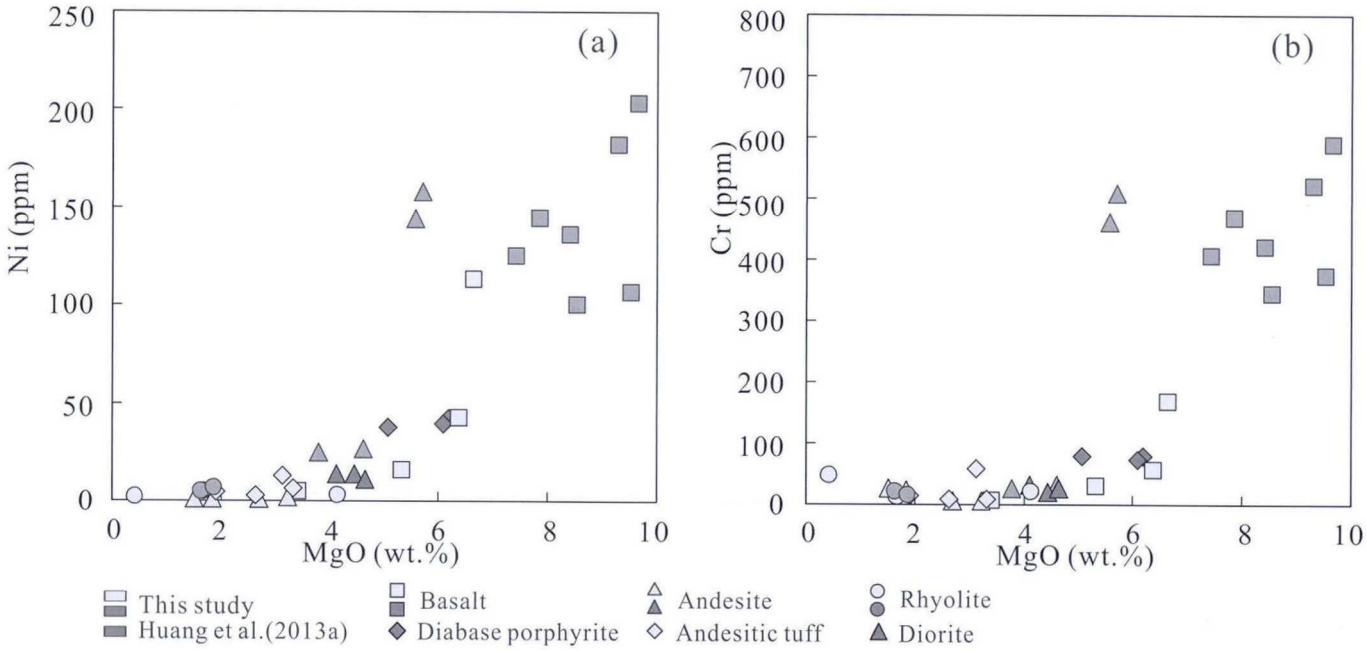


**Figure 12.** Tectonic discrimination diagrams for the Shaquanzi diorite. (a) Ta vs. Yb and (b) Rb vs. Y + Nb (after Pearce et al., 1984). ORG = Ocean Ridge Granite; WPG = Within Plate Granite; VAG = Volcanic Arc Granite; syn-COLG = Syn-Collisional Granite.

BABB/MORB, with two data points falling into the overlapping field of IAB and BABB/MORB (Fig. 13c). In the FeO*/MgO vs. $TiO_2$ diagram (Fig. 13d) (Shuto et al., 2006), these samples fall predominantly into the BABB field. In the Ti/Zr vs. Zr diagram (Fig. 13e) (Wang et al., 2013b), most (except for one) of the Shaquanzi mafic rocks also plot in the BABB field. Furthermore, Ba/Yb correlates negatively to Ba/Nb for IAB (Pearce et al., 1995), but positive for BABB (Leat et al., 2000), which occurs in the Ba/Yb ratios of the Shaquanzi mafic rocks (Fig. 13f). Furthermore, the REE patterns and primitive mantle-normalized patterns of the Shaquanzi Formation basaltic- and rhyolitic rocks are very similar to Okinawa Trough BAB basalt and rhyolite, respectively, but distinct from the typical arc volcanics from Barren Island Volcano (Fig. 6) (Shinjo et al., 1999; Shinjo and Kato, 2000; Luhr and Haldar, 2006). The $\varepsilon_{Nd}(t)$ isotope

compositions are also comparable to those of typical BAB volcanic rocks, but distinct from the typical arc volcanics (Fig. 7a). All these features indicate a BAB setting for these Shaquanzi Formation rocks.

This study also investigates whether the proposed BAB was developed on an intra-continental arc or an intra-oceanic arc. Intra-continental BABBs commonly exhibit $(La/Yb)_N > 3$, $Ba/La > 10$ and $Sm/Nd < 0.3$ (Hickey-Vargas et al., 1995; Shinjo et al., 1999; Fan et al., 2010). The Shaquanzi Formation mafic rocks have $(La/Yb)_N = 1.53–6.38$, $Ba/La = 13.08–42.65$ and $Sm/Nd = 0.226–0.296$, clearly resemble typical intra-continental BABBs, as in the case of some intra-continental BABB from the Western Pacific (Fan et al., 2010). Moreover, Shaquanzi Formation mafic rocks show different primitive mantle-normalized multi-element and chondrite-normalized REE patterns from the intra-oceanic Lesser Caucasus BABB (Rolland et al., 2009), but similar to the intra-continental Okinawa Trough back-arc basin mafic rocks (Fig. 6a and b) (Shinjo et al., 1999). Therefore, the LILEs enrichment, HFSEs depletion

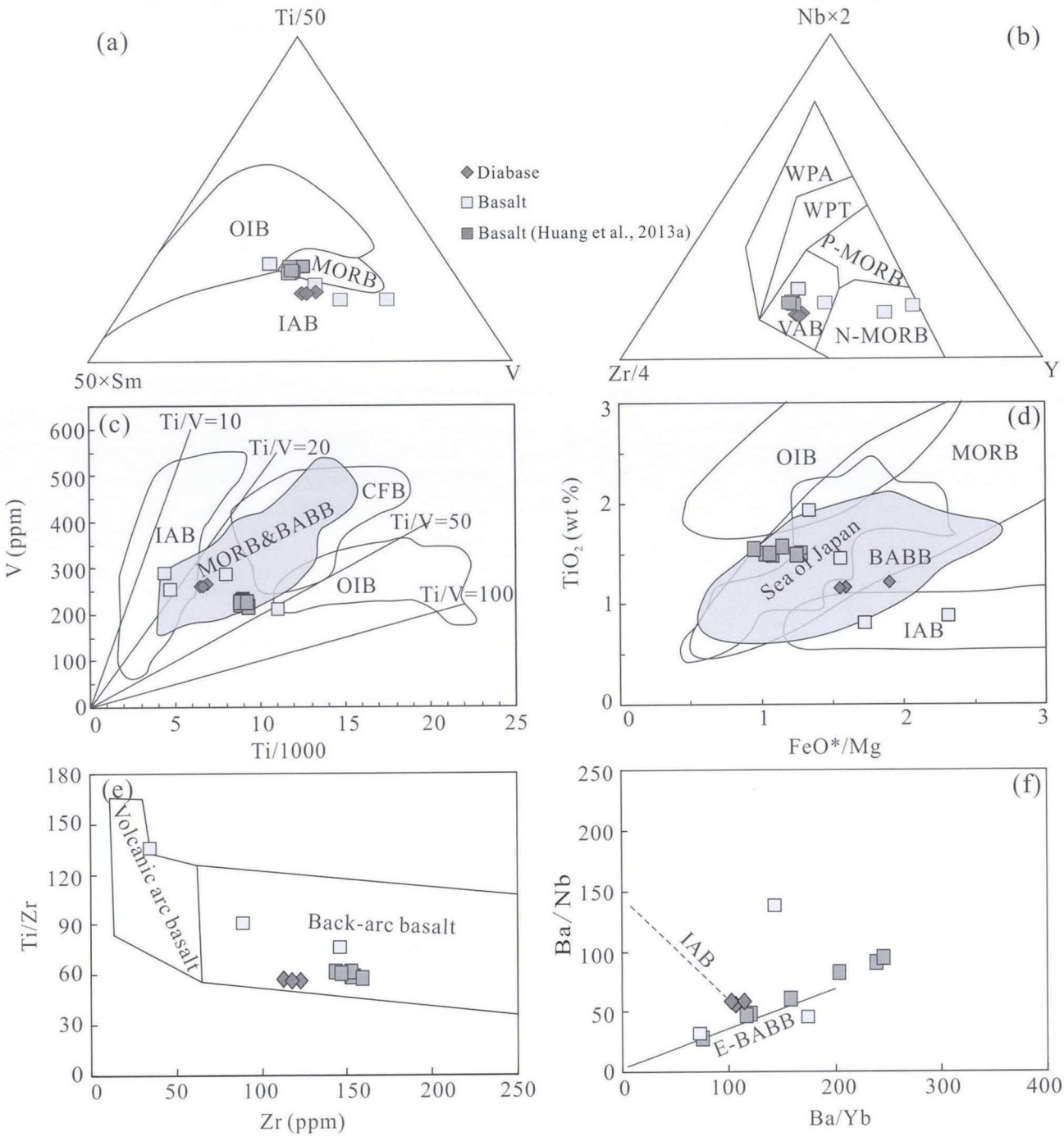


**Figure 13.** Tectonic discrimination diagrams for the Shaquanzi Formation basaltic rocks. (a) Ti/50 – 50 × Sm–V ternary diagram after Vermeesch (2006); (b) 2 × Nb–Zr/4–Y ternary diagram after Meschede (1986); (c) V vs. Ti/1000 after Shervais (1982); (d) $TiO_2$ vs. FeO*/MgO after Shuto et al. (2006); (e) Ti/Zr vs. Zr after Wang et al. (2013b) and (f) Ba/Nb vs. Ba/Yb after Leat et al. (2000) and Li et al. (2013). WPA = Within-Plate Alkaline Basalts; WPT = Within-Plate Tholeiites; VAB = Volcanic Arc Basalts; N-MORB = Normal Mid-Ocean Ridge Basalt; E-MORB = Enriched-MORB.

and slightly enriched Sr-Nd isotopes of the Shaquanzi Formation rocks are more comparable with intra-continental BABBs (Gribble et al., 1998; Sandeman et al., 2006).

The intra-continental BAB setting for the Shaquanzi volcanic rocks is also supported by the following lines of evidence: (1) the Carboniferous marine fossils (e.g., *Dibunophyllum cf.* and *Profusulinella* sp.) from the limestone of Yamansu and Shaquanzi formations (Zhang et al., 2012) indicate the existence of a Carboniferous oceanic basin (Kanggur ocean basin) in the Yamansu belt; (2) ophiolites along the Kanggur Fault represents remnants of the Kanggur ocean basin (Li et al., 2006); (3) studies on the submarine volcanic-hosted iron oxide deposits in the Yamansu belt reveal their formation in an extensional setting (Wang et al., 2006; Xu et al., 2011); (4) the bimodal Yamansu Formation volcanic rocks, documented in the western and middle part of the Jueluotage belt (Chen et al., 2003), also indicate an extensional setting; (5) inherited zircons from felsic rocks of the Yamansu Formation with similar age peaks (ca. 900 and 1400 Ma) and the crystallization age of the Middle Tianshan Massif (Luo et al., 2012), indicate that the Yamansu belt possibly developed on the northern margin of the Middle Tianshan Massif. This also supports the south-dipping subduction of the Kangguer Ocean beneath the Middle Tianshan Massif, and is consistent with the study of the volcanic rocks of the Lower Carboniferous Yamansu Formation which show continental arc geochemical affinity (Hou et al., 2006). All these features suggest a back-arc extension setting developed on a continental arc and the Yamansu Formation (ca. 348–324 Ma) (Luo et al., 2012; Zhang et al., 2012; Hou et al., 2014b) might have formed during the arc to incipient back-arc rifting stage, and the Shaquanzi Formation might have formed during the mature back-arc basin formation stage. As a result, we propose that the Yamansu belt was under an arc to back-arc basin transition in the Carboniferous.

In the Early Carboniferous, the south-dipping subduction of the Kangguer Ocean might have existed beneath the Middle Tianshan Massif, giving rise to continental arc magmatism that formed the calc-alkaline felsic rocks of the Yamansu Formation (ca. 348–334 Ma) (Hou et al., 2006; Luo et al., 2012; Zhang et al., 2012) and several granitoids in the western Yamansu mineralization belt (ca. 349–337 Ma) (Zhou et al., 2010; Fig. 14a). Accompanied with the emplacement of Hongyuntan granodiorite (ca. 329 Ma), arc rifting occurred and formed the upper Yamansu Formation bimodal volcanic rocks (ca. 334–324 Ma) (Chen et al., 2003; Zhou et al., 2010; Hou et al., 2014b; Fig. 14b). In the Late Carboniferous, followed by the intrusion of the Bailingshan granodiorite pluton (ca. 318 Ma), continuous back-arc extension might have led to the emplacement of the Shaquanzi Formation volcanic rocks (ca. 322–305 Ma) (Zhou et al., 2010; Xu et al., 2014 and this study). The youngest age (ca. 298 Ma) and volcanic-arc features of the

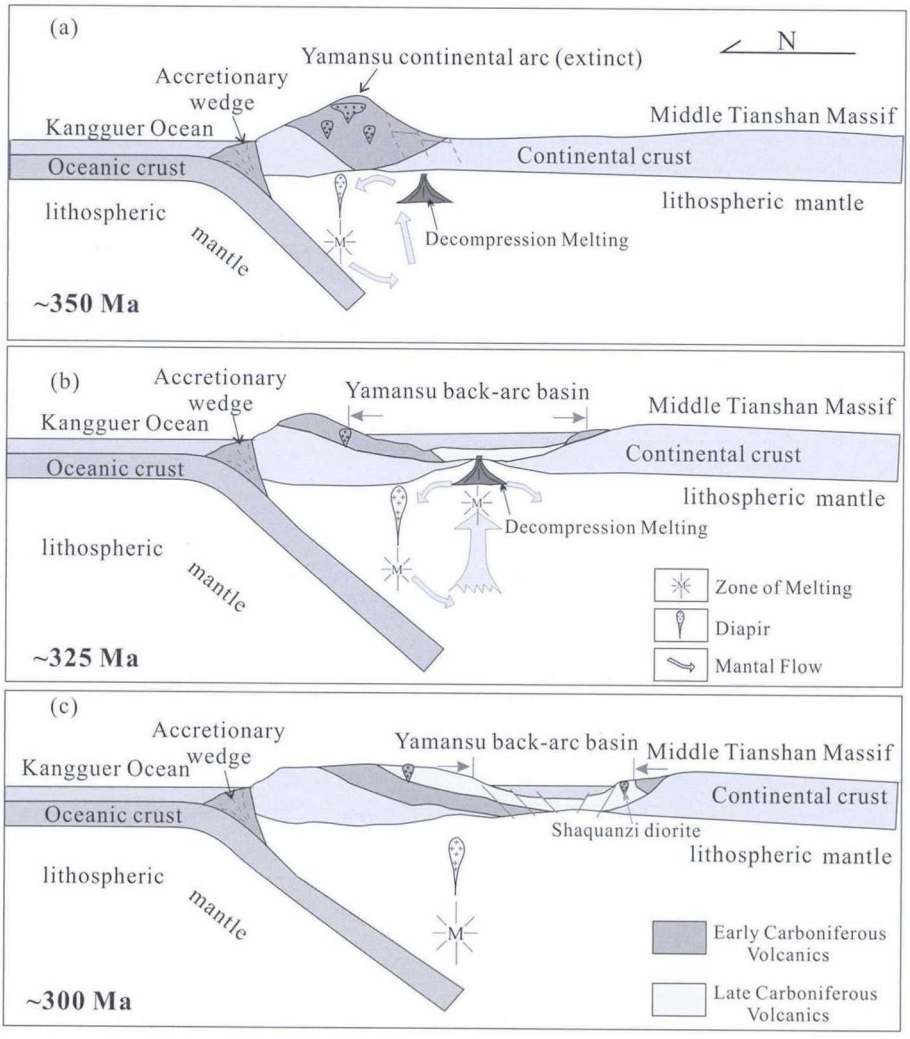


**Figure 14.** Schematic model showing the development of the Carboniferous arc–back-arc system along the Yamansu belt.

Shaquanzi diorite, similar to many intermediate-felsic intrusions formed along the Aqikekuduke-Shaquanzi Fault between the Yamansu belt and the Central Tianshan Massif, indicate the Yamansu back-arc basin might have closed and the area evolved into an arc system again in the Early Permian (Fig. 14c), which is consistent with the hypothesis that the subduction of the Kangguer ocean may have ceased in the Late Carboniferous to Early Permian (Xiao et al., 2004), supported by the 300 Ma shear zone-hosted Au deposits and the 280 Ma Xiangshan Ni-Cu-Co deposit in the Kangguer ductile metamorphosed belt formed during syn- and post-accretion (Han et al., 2010).

## 7. Conclusions

(1) LA-ICP-MS zircon U-Pb geochronology indicates that the Shaquanzi Formation volcanic rocks in the Yamansu belt formed in the Late Carboniferous (315–305 Ma), and the diorite formed in the Early Permian (298 Ma).
(2) The primary magma of the Shaquanzi Formation basaltic rocks might have been derived from the depleted, metasomatized lithospheric mantle with minor (3–5%) subduction-related material input, whereas the andesites and rhyolites likely to be the fractional crystallization products of the basaltic magma.
(3) The Yamansu belt might have evolved from a continental arc to a back-arc basin setting during the Late Carboniferous and the continuous back-arc extension might have led to the emplacement of the Shaquanzi Formation volcanic rocks.

## Acknowledgements

We are grateful to Dr. Bing Xiao and Weifeng Zhang for the fruitful discussion and modification of the manuscript. Field work was assisted by the No. 6 Geological Party, Xinjiang Bureau of Geology and Mineral Exploration and their help in the field is acknowledged. We also appreciate the laboratory assistance guidance offered by Jinlong Ma, Le Zhang and Congying Li from Guangzhou Institute of Geochemistry, Chinese Academy of Sciences (GIGCAS). This study was financially supported by the Chinese National Basic Research 973-Program (No. 2014CB440802). This is contributed to Project No. IS-2353 of GIGCAS.

## Appendix A. Supplementary data

Supplementary data related to this article can be found at http://dx.doi.org/10.1016/j.gsf.2017.01.008.

## References

Ayalew, D., Yirgu, G., 2003. Crustal contribution to the genesis of Ethiopian plateau rhyolitic ignimbrites: basalt and rhyolite geochemical provinciality. Journal of the Geological Society 160, 47–56.
Bacon, C.R., Druitt, T.H., 1988. Compositional evolution of the zoned calcalkaline magma chamber of Mount Mazama, Crater Lake, Oregon. Contributions to Mineralogy and Petrology 98, 224–256.
Black, L.P., Kamo, S.L., Allen, C.M., Aleinikoff, J.N., Davis, D.W., Korsch, R.J., Foudoulis, C., 2003. TEMORA 1: a new zircon standard for Phanerozoic U-Pb geochronology. Chemical Geology 200, 155–170.
Bonin, B., 2004. Do coeval mafic and felsic magmas in post-collisional to within-plate regimes necessarily imply two contrasting, mantle and crustal, sources? A review. Lithos 78, 1–24.
Bouvier, A., Vervoort, J.D., Patchett, P.J., 2008. The Lu-Hf and Sm-Nd isotopic composition of CHUR: constraints from unequilibrated chondrites and implications for the bulk composition of terrestrial planets. Earth and Planetary Science Letters 273, 48–57.
Cai, T.C., 1999. Stratigraphy of Xinjiang Uygur Autonomous Region. China University of Geosciences Press, Wuhan (in Chinese).
Charvet, J., Shu, L.S., Laurent-Charvet, S., Wang, B., Faure, M., Cluzel, D., Chen, Y., De Jong, K., 2011. Palaeozoic tectonic evolution of the Tianshan belt, NW China. Science China Earth Sciences 54, 166–184.
Chen, B., Jahn, B.M., Tian, W., 2009. Evolution of the Solonker suture zone: constraints from zircon U-Pb ages, Hf isotopic ratios and whole-rock Nd-Sr isotope compositions of subduction-and collision-related magmas and forearc sediments. Journal of Asian Earth Sciences 34, 245–257.
Chen, F.W., He, G.Q., Li, H.Q., 2003. Tectonic attribute of Qoltag orogenic belt in the Eastern Tianshan Mountains, northwestern China. Geology in China 30 (4), 361–366 (in Chinese with English abstract).
Chen, L., Zhao, Z.F., Zheng, Y.F., 2014. Origin of andesitic rocks: geochemical constraints from Mesozoic volcanics in the Luzong basin, South China. Lithos 190, 220–239.
Chen, X.J., Shu, L.S., Santosh, M., Zhao, X.X., 2013. Island arc-type bimodal magmatism in the eastern Tianshan Belt, Northwest China: geochemistry, zircon U-Pb geochronology and implications for the Paleozoic crustal evolution in Central Asia. Lithos 168, 48–66.
Chu, N.C., Taylor, R.N., Chavagnac, V., Nesbitt, R.W., Boella, R.M., Milton, J.A., German, C.R., Bayon, G., Burton, K., 2002. Hf isotope ratio analysis using multi-collector inductively coupled plasma mass spectrometry: an evaluation of isobaric interference corrections. Journal of Analytical Atomic Spectrometry 17, 1567–1574.
Condie, K.C., 2005. High field strength element ratios in Archean basalts: a window to evolving sources of mantle plumes? Lithos 79, 491–504.
Fan, W.M., Wang, Y.J., Zhang, A.M., Zhang, F.F., Zhang, Y.Z., 2010. Permian arc-back-arc basin development along the Ailaoshan tectonic zone: geochemical, isotopic and geochronological evidence from the Mojiang volcanic rocks, Southwest China. Lithos 119, 553–568.
Frey, F.A., Green, D.H., Roy, S.D., 1978. Integrated models of basalt petrogenesis: a study of quartz tholeiites to olivine melilitites from south eastern Australia utilizing geochemical and experimental petrological data. Journal of Petrology 19, 463–513.
Gao, S., Liu, X.M., Yuan, H.L., Hattendorf, B., Gunther, D., Chen, L., Hu, S.H., 2002. Determination of forty two major and trace elements in USGS and NIST SRM glasses by laser ablation-inductively coupled plasma-mass spectrometry. Geostandards Newsletter-the Journal of Geostandards and Geoanalysis 26, 181–196.
Green, D.H., 1973. Experimental melting studies on a model upper mantle composition at high pressure under water-saturated and water-undersaturated conditions. Earth and Planetary Science Letters 19, 37–53.
Gribble, R.F., Stern, R.J., Newman, S., Bloomer, S.H., O'Hearn, T., 1998. Chemical and isotopic composition of lavas from the northern Mariana Trough: implications for magmagenesis in back-arc basins. Journal of Petrology 39, 125–154.
Griffin, W.L., Pearson, N.J., Belousova, E., Jackson, S.E., Van Achterbergh, E., O'Reilly, S.Y., Shee, S.R., 2000. The Hf isotope composition of cratonic mantle: LA-MC-ICPMS analysis of zircon megacrysts in kimberlites. Geochimica Et Cosmochimica Acta 64, 133–147.
Griffin, W.L., Wang, X., Jackson, S.E., Pearson, N.J., O'Reilly, S.Y., Xu, X.S., Zhou, X.M., 2002. Zircon chemistry and magma mixing, SE China: in-situ analysis of Hf isotopes, Tonglu and Pingtan igneous complexes. Lithos 61, 237–269.
Guffanti, M., Clynne, M.A., Muffler, L.J., 1996. Thermal and mass implications of magmatic evolution in the Lassen volcanic region, California, and minimum constraints on basalt influx to the lower crust. Journal of Geophysical Research: Solid Earth (1978–2012) 101, 3003–3013.
Han, C.M., Xiao, W.J., Zhao, G.C., Ao, S.J., Zhang, J., Qu, W.J., Du, A.D., 2010. In-situ U–Pb, Hf and Re–Os isotopic analyses of the Xiangshan Ni–Cu–Co deposit in eastern Tianshan (Xinjiang), central Asia Orogenic Belt: constraints on the timing and genesis of the mineralization. Lithos 120 (3), 547–562.
Hart, S.R., 1984. A large-scale isotope anomaly in the Southern Hemisphere mantle. Nature 309, 753–757.
Hastie, A.R., Kerr, A.C., Pearce, J.A., Mitchell, S.F., 2007. Classification of altered volcanic island arc rocks using immobile trace elements: development of the Th-Co discrimination diagram. Journal of Petrology 48, 2341–2357.
Hanson, G.N., Langmuir, C.H., 1978. Modelling of major elements in mantle-melt systems using trace element approaches. Geochimica et Cosmochimica Acta 42, 725–741.
Hickey-Vargas, R., Hergt, J.M., Spadea, P., 1995. The Indian Ocean-type isotopic signature in western Pacific marginal basins: origin and significance. Active Margins and Marginal Basins of the Western Pacific 175–197.
Hou, G.S., Tang, H.F., Liu, C.Q., 2006. Geochemical characteristics of the Late Paleozoic volcanics in Jueluotage tectonic belt, eastern Tianshan and its implications. Acta Petrologica Sinica 22 (5), 1167–1177 (in Chinese with English abstract).
Hou, G.S., Tang, H.F., Liu, C.Q., 2007. Study on the mineralogy of vocanics of the Yamanshu group in the Juoluotage Tectonic Belt, east Tianshan. Acta Mineralogica Sinica 27 (2), 189–194 (in Chinese with English abstract).
Hou, G.S., Tang, H.F., Liu, C.Q., Wang, Y.B., 2005. Geochronological and geochemical study on the wallrocks of Tuwu-Yandong porphyry copper deposits, Eastern Tianshan Mountains. Acta Petrologia Sinica 21 (6), 1729–1736 (in Chinese with English abstract).
Hou, T., Zhang, Z.C., Pirajno, F., Santosh, M., Encarnacion, J., Liu, J.L., Zhao, Z.D., Zhang, L.J., 2014a. Geology, tectonic settings and iron ore metallogenesis associated with submarine volcanism in China: an overview. Ore Geology Reviews 57, 498–517.
Hou, T., Zhang, Z.C., Santosh, M., Encarnacion, J., Zhu, J., Luo, W.J., 2014b. Geochronology and geochemistry of submarine volcanic rocks in the Yamansu iron deposit, Eastern Tianshan Mountains, NW China: constraints on the metallogenesis. Ore Geology Reviews 56, 487–502.

Hoang, N., Uto, K., 2006. Upper mantle isotopic components beneath the Ryukyu arc system: evidence for 'back-arc' entrapment of Pacific MORB mantle. Earth and Planetary Science Letters 249, 229–240.

Huang, P., Li, C.A., Jiang, H.Y., 2006. Geochemical features and their geological implications of volcanic rocks from the northern and middle Okinawa Trough. Acta Petrologica Sinica 22 (6), 1703–1712 (in Chinese with English abstract).

Huang, X.W., Qi, L., Gao, J.F., Liu, Y.Y., Wang, Y.C., 2013a. Geochemistry of volcanic rocks in the Dikan'er Formation of Jueluotage region, Eastern Tianshan Mountains and its tectonic implications. Acta Petrologica et Mineralogiga 31 (6), 799–817 (in Chinese with English abstract).

Huang, X.W., Qi, L., Gao, J.F., Zhao, Z., 2012. Geochemistry of platinum-group (PGEs) in Carboniferous volcanic rocks from the Shaquanzi area, east Tianshan, Xinjiang, China. Bulletin of Mineralogy, Petrology and Geochemistry 31 (6), 575–589 (in Chinese with English abstract).

Huang, X.W., Qi, L., Gao, J.F., Zhou, M.F., 2013b. First reliable Re-Os ages of pyrite and stable isotope compositions of Fe (-Cu) deposits in the Hami region, eastern Tianshan orogenic belt, NW China. Resource Geology 63, 166–187.

Huang, X.W., Qi, L., Meng, Y.M., 2014a. Trace element geochemistry of magnetite from the Fe (-Cu) deposits in the Hami Region, eastern Tianshan Orogenic Belt, NW China. Acta Geologica Sinica-English Edition 88, 176–195.

Huang, X.W., Qi, L., Wang, Y.C., Liu, Y.Y., 2014b. Re-Os dating of magnetite from the Shaquanzi Fe-Cu deposit, eastern Tianshan, NW China. Science China Earth Sciences 57, 267–277.

Ji, J.S., Tao, H.X., Yang, X.K., 1994. Geochemical characteristics of volcanic rocks within different tectonic setting in the central part of East Tianshan. Acta Petrologica Et Mineralogiga 13 (4), 297–304 (in Chinese with English abstract).

Kang, Z.Q., Xu, J.F., Wilde, S.A., Feng, Z.H., Chen, J.L., Wang, B.D., Fu, W.C., Pan, H.B., 2014. Geochronology and geochemistry of the Sangri group volcanic rocks, southern Lhasa Terrane: implications for the early subduction history of the neo-Tethys and Gangdese Magmatic Arc. Lithos 200, 157–168.

Kelley, K.A., Cottrell, E., 2012. The influence of magmatic differentiation on the oxidation state of Fe in a basaltic arc magma. Earth and Planetary Science Letters 329, 109–121.

Koschek, G., 1993. Origin and significance of the sem cathodoluminescence from zircon. Journal of Microscopy-Oxford 171, 223–232.

Leat, P.T., Livermore, R.A., Millar, I.L., Pearce, J.A., 2000. Magma supply in back-arc spreading centre segment E2, East Scotia Ridge. Journal of Petrology 41, 845–866.

Li, B., Bagas, L., Gallardo, L.A., Said, N., Diwu, C., McCuaig, T.C., 2013. back-arc and post-collisional volcanism in the palaeoproterozoic granites-Tanami Orogen, Australia. Precambrian Research 224, 570–587.

Li, C.Y., Zhang, H., Wang, F.Y., Liu, J.Q., Sun, Y.L., Hao, X.L., Li, Y.L., Sun, W.D., 2012. The formation of the Dabaoshan porphyry molybdenum deposit induced by slab rollback. Lithos 150, 101–110.

Li, J.Y., 2004. Late Neoproterozoic and Paleozoic tectonic framework and evolution of eastern Xinjiang. Geological Review 50 (3), 304–322 (in Chinese with English abstract).

Li, J.Y., Wang, K.Z., Sun, G.H., Mo, S.G., Li, W.Q., Yang, T.N., Gao, L.M., 2006. Paleozoic active margin slices in the southern Turfan–Hami basin: geological records of subduction of the Paleo-Asian ocean plate in Central Asian regions. Acta Petrologica Sinica 22, 1087–1102 (in Chinese with English abstract).

Li, L., Zheng, Y.F., Zhou, J.B., 2001. Dynamic model for Pb isotope evolution in the continental crust of China. Acta Petrologica Sinica 17, 61–68 (in Chinese with English abstract).

Li, X.M., Xia, Z.C., Xu, X.Y., Ma, Z.P., Wang, L.S., 2005. Zirocn U-Pb geochronology of volcanic rocks of the Qi'eshan Group in the east Tianshan Mountains. Geological Bulletin of China 23, 1215–1220 (in Chinese with English abstract).

Li, Y., Yang, J.S., Zhang, J., Li, T.F., Chen, S.Y., Ren, Y.F., Xu, X.Z., 2011. Tectonic significance of the Carboniferous volcanicrocks in eastern Tianshan. Acta Petrologica Sinica 27 (1), 193–209 (in Chinese with English abstract).

Liang, J.L., Ding, X., Sun, X.M., Zhang, Z.M., Zhang, H., Sun, W.D., 2009. Nb/Ta fractionation observed in eclogites from the Chinese continental scientific Drilling Project. Chemical Geology 268, 27–40.

Liu, S.W., Guo, Z.J., Zhang, Z.C., Li, Q.G., Zheng, H.F., 2004. Nature of the Precambrian metamorphic blocks in the eastern segment of Central Tianshan: constraint from geochronology and Nd isotopic geochemistry. Science in China Series D: Earth Sciences 47, 1085–1094.

Liu, Y.S., Gao, S., Hu, Z.C., Gao, C.G., Zong, K.Q., Wang, D.B., 2010. Continental and oceanic crust recycling-induced melt-peridotite interactions in the Trans-North China Orogen: U-Pb dating, Hf isotopes and trace elements in zircon grains from mantle xenoliths. Journal of Petrology 51, 537–571.

Liu, Y.S., Hu, Z.C., Gao, S., Guenther, D., Xu, J., Gao, C.G., Chen, H.H., 2008. In situ analysis of major and trace elements of anhydrous minerals by LA-ICP-MS without applying an internal standard. Chemical Geology 257, 34–43.

Ludwig, K., 2003. User's Manual for Isoplot/Ex version 3.00—A Geochronology Toolkit for Microsoft Excel, No. 4. Berkeley Geochronological Center, Special Publication.

Luhr, J.F., Haldar, D., 2006. Barren Island Volcano (NE Indian Ocean): island-arc high alumina basalts produced by troctolite contamination. Journal of Volcanology and Geothermal Research 149, 177–212.

Luo, T., Liao, Q.A., Chen, J.P., Zhang, X.H., Guo, D.B., Hu, Z.C., 2012. LA-ICP-MS zircon U-Pb dating of the volcanic rocks from Yamansu Formation in the eastern Tianshan, and its geological significance. Earth Science-Journal of China University of Geosciences 37 (6), 1338–1552 (in Chinese with English abstract).

Ma, R.S., Wang, C.Y., Ye, S.F., 1993. Tectonic Framework and Crustal Evolution of Eastern Tianshan. Nanjing University Press, Nanjing (in Chinese).

Machado, N., Simonetti, A., 2001. U-Pb dating and Hf isotopic composition of zircon by laser ablation-MC-ICP-MS. Laser-Ablation-Icpms in the Earth Sciences 29, 121–146.

Mao, J.W., Goldfarb, R.J., Wang, Y.T., Hart, C.J., Wang, Z.L., Yang, J.M., 2005. Late Paleozoic base and precious metal deposits, East Tianshan, Xinjiang, China: characteristics and geodynamic setting. Episodes-Newsmagazine of the International Union of Geological Sciences 28, 23–30.

Meng, X.W., Du, D.W., Wu, J.L., Long, J.P., 1999. Sr-Nd isotope features and their geological implications of vocanic rocks from middle Okinawa Trough. Science in China (Series D) 29 (4), 367–371 (in Chinese).

Meschede, M., 1986. A method of discriminating between different types of mid-ocean ridge basalts and continental tholeiites with the Nb-Zr-Y diagram. Chemical Geology 56, 207–218.

Pearce, J.A., 2008. Geochemical fingerprinting of oceanic basalts with applications to ophiolite classification and the search for Archean oceanic crust. Lithos 100, 14–48.

Pearce, J.A., Baker, P.E., Harvey, P.K., Luff, I.W., 1995. Geochemical evidence for subduction fluxes, mantle melting and fractional crystallization beneath the South Sandwich island arc. Journal of Petrology 36, 1073–1109.

Pearce, J.A., Harris, N.B.W., Tindle, A.G., 1984. Trace element discrimination diagrams for the tectonic interpretation of granitic rocks. Journal of Petrology 25, 956–983.

Pearce, J.A., Stern, R.J., 2006. Origin of back-arc basin magmas: trace element and isotope perspectives. Back-Arc Spreading Systems: Geological, Biological, Chemical, and Physical Interactions 63–86.

Pearce, J.A., Stern, R.J., Bloomer, S.H., Fryer, P., 2005. Geochemical mapping of the Mariana arc-basin system: implications for the nature and distribution of subduction components. Geochemistry, Geophysics, Geosystems 6.

Pearce, N.J.G., Perkins, W.T., Westgate, J.A., Gorton, M.P., Jackson, S.E., Neal, C.R., Chenery, S.P., 1997. A compilation of new and published major and trace element data for NIST SRM 610 and NIST SRM 612 glass reference materials. Geostandards Newsletter-the Journal of Geostandards and Geoanalysis 21, 115–144.

Perfit, M.R., Gust, D.A., Bence, A.E., Arculus, R.J., Taylor, S.R., 1980. Chemical characteristics of island-arc basalts: implications for mantle sources. Chemical Geology 30, 227–256.

Pin, C., Paquette, J.L., 1997. A mantle-derived bimodal suite in the Hercynian Belt: Nd isotope and trace element evidence for a subduction-related rift origin of the Late Devonian Brévenne metavolcanics, Massif Central (France). Contributions to Mineralogy and Petrology 129, 222–238.

Plank, T., Langmuir, C.H., 1998. The chemical composition of subducting sediment and its consequences for the crust and mantle. Chemical Geology 145, 325–394.

Qian, Y., Ge, W.C., Yang, H., Zhao, G.C., Zhang, Y.L., Su, L., 2014. Petrogenesis of late Paleozoic volcanic rocks from the Daheshen Formation in central Jilin Province, NE China, and its tectonic implications: constraints from geochronology, geochemistry and Sr-Nd-Hf isotopes. Lithos 192, 116–131.

Qin, K.Z., Fang, T.H., Wang, S.L., Zhu, B.Q., Feng, Y.M., Yu, H.F., Xiu, Q.Y., 2002. Plate tectonics division, evolution and metallogenic setting in Eastern Tianshan Mountains, NE-China. Xinjiang Geology 20 (4), 302–308 (in Chinese with English abstract).

Qin, K.Z., Su, B.X., Sakyi, P.A., Tang, D.M., Li, X.H., Sun, H., Xiao, Q.H., Liu, P.P., 2011. SIMS zircon U-Pb geochronology and Sr-Nd isotopes of Ni-Cu-bearing Mafic-Ultramafic Intrusions in Eastern Tianshan and Beishan in correlation with flood basalts in Tarim Basin (NW China): constraints on a ca. 280 Ma mantle plume. American Journal of Science 311, 237–260.

Riley, T., Leat, P.T., Pankhurst, R.J., Harris, C., 2001. Origins of large volume rhyolitic volcanism in the Antarctic Peninsula and Patagonia by crustal melting. Journal of Petrology 42, 1043–1065.

Roberts, M.P., Clemens, J.D., 1993. Origin of high-potassium, talc-alkaline, I-type granitoids. Geology 21, 825–828.

Rolland, Y., Galoyan, G., Bosch, D., Sosson, M., Corsini, M., Fornari, M., Verati, C., 2009. Jurassic back-arc and Cretaceous hot-spot series in the Armenian ophiolites—implications for the obduction process. Lithos 112, 163–187.

Rudnick, R.L., Fountain, D.M., 1995. Nature and composition of the continental crust: a lower crustal perspective. Reviews of Geophysics 33, 267–309.

Rudnick, R.L., Gao, S., 2003. Composition of the continental crust. Treatise on Geochemistry 3, 1–64.

Said, N., Kerrich, R., 2009. Geochemistry of coexisting depleted and enriched Paringa Basalts, in the 2.7 Ga Kalgoorlie Terrane, Yilgarn Craton, Western Australia: evidence for a heterogeneous mantle plume event. Precambrian Research 174, 287–309.

Sandeman, H.A., Hanmer, S., Tella, S., Armitage, A.A., Davis, W.J., Ryan, J.J., 2006. Petrogenesis of Neoarchaean volcanic rocks of the MacQuoid supracrustal belt: a back-arc setting for the northwestern Hearne subdomain, western Churchill Province, Canada. Precambrian Research 144, 140–165.

Saunders, A.D., Tarney, J., 1984. Geochemical characteristics of basaltic volcanism within back-arc basins. Geological Society, London, Special Publications 16, 59–76.

Şengör, A.M.C., Natal'in, B.A., Burtman, U.S., 1993. Evolution of the Altaid tectonic collage and Paleozoic crustal growth in Eurasia. Nature 364, 209–304.

Shervais, J.W., 1982. Ti-V plots and the petrogenesis of modern and ophiolitic lavas. Earth and Planetary Science Letters 59, 101–118.

Shinjo, R., Chung, S.L., Kato, Y., Kimura, M., 1999. Geochemical and Sr-Nd isotopic characteristics of volcanic rocks from the Okinawa Trough and Ryukyu arc: implications for the evolution of a young, intracontinental back arc basin. Journal of Geophysical Research-Solid Earth 104, 10591–10608.

Shinjo, R., Kato, Y., 2000. Geochemical constraints on the origin of bimodal magmatism at the Okinawa Trough, an incipient back-arc basin. Lithos 54, 117–137.

Shuto, K., Ishimoto, H., Hirahara, Y., Sato, M., Matsui, K., Fujibayashi, N., Takazawa, E., Yabuki, K., Sekine, M., Kato, M., 2006. Geochemical secular variation of magma source during Early to Middle Miocene time in the Niigata area, NE Japan: asthenospheric mantle upwelling during back-arc basin opening. Lithos 86, 1–33.

Soderlund, U., Patchett, J.P., Vervoort, J.D., Isachsen, C.E., 2004. The Lu-176 decay constant determined by Lu-Hf and U-Pb isotope systematics of Precambrian mafic intrusions. Earth and Planetary Science Letters 219, 311–324.

Su, B.X., Qin, K.Z., Sakyi, P.A., Li, X.H., Yang, Y.H., Sun, H., Tang, D.M., Liu, P.P., Xiao, Q.H., Malaviarachchi, S.P., 2011. U-Pb ages and Hf-O isotopes of zircon grains from Late Paleozoic mafic-ultramafic units in the southern Central Asian Orogenic Belt: tectonic implications and evidence for an Early-Permian mantle plume. Gondwana Research 20, 516–531.

Su, B.X., Qin, K.Z., Sun, H., Tang, D.M., Sakyi, P.A., Chu, Z.Y., Liu, P.P., Xiao, Q.H., 2012. Subduction-induced mantle heterogeneity beneath eastern Tianshan and Beishan: insights from Nd-Sr-Hf-O isotopic mapping of Late Paleozoic mafic-ultramafic complexes. Lithos 134, 41–51.

Sun, S.S., McDonough, W.F., 1989. Chemical and isotopic systematics of oceanic basalts: implications for mantle composition and processes. Geological Society, London, Special Publications 42, 313–345.

Tu, X.L., Zhang, H., Deng, W.F., Ling, M.X., Liang, H.Y., Liu, Y., Sun, W.D., 2011. Application of resolution in-situ laser ablation ICP-MS in trace element analyses. Geochimica 40, 83–98.

Vermeesch, P., 2006. Tectonic discrimination diagrams revisited. Geochemistry, Geophysics, Geosystems 7.

Wang, H., Wu, Y.B., Qin, Z.W., Zhu, L.Q., Liu, Q., Liu, X.C., Gao, S., Wijbrans, J.R., Zhou, L., Gong, H.J., 2013a. Age and geochemistry of Silurian gabbroic rocks in the Tongbai orogen, central China: implications for the geodynamic evolution of the North Qinling arc-back-arc system. Lithos 179, 1–15.

Wang, J.B., Wang, Y.W., He, Z.J., 2006. Ore deposits as a guide to the tectonic evolution in the East Tianshan Mountains, NW China. Geology in China 33 (3), 461–469 (in Chinese with English abstract).

Wang, Y.J., Zhang, A.M., Cawood, P.A., Fan, W.M., Xu, J.F., Zhang, G.W., Zhang, Y.Z., 2013b. Geochronological, geochemical and Nd-Hf-Os isotopic fingerprinting of an early Neoproterozoic arc-back-arc system in South China and its accretionary assembly along the margin of Rodinia. Precambrian Research 231, 343–371.

Wang, Y.H., Xue, C.J., Liu, J.J., Wang, J.P., Yang, J.T., Zhang, F.F., Zhao, Z.N., Zhao, Y.J., Liu, B., 2015. Early Carboniferous adakitic rocks in the area of the Tuwu deposit, eastern Tianshan, NW China: slab melting and implications for porphyry copper mineralization. Journal of Asian Earth Sciences 103, 332–349.

Wilkinson, J.F.G., Le Maitre, R.W., 1987. Upper mantle amphiboles and micas and $TiO_2$, $K_2O$, and $P_2O_5$ abundances and 100 $Mg/(Mg+ Fe^{2+})$ ratios of common basalts and andesites: implications for modal mantle metasomatism and undepleted mantle compositions. Journal of Petrology 28, 37–73.

Wilson, M., 1993. Magmatism and the geodynamics of basin formation. Sedimentary Geology 86, 5–29.

Winchester, J.A., Floyd, P.A., 1976. Geochemical magma type discrimination: application to altered and metamorphosed basic igneous rocks. Earth and Planetary Science Letters 28, 459–469.

Winchester, J.A., Floyd, P.A., 1977. Geochemical discrimination of different magma series and their differentiation products using immobile elements. Chemical Geology 20, 325–343.

Woodhead, J.D., Hergt, J.M., Davidson, J.P., Eggins, S.M., 2001. Hafnium isotope evidence for 'conservative' element mobility during subduction zone process. Earth and Planetary Science Letters 192, 331–346.

Xia, L.Q., Xu, X.Y., Xia, Z.C., Li, X.M., Ma, Z.P., Wang, L.S., 2003. Carboniferous post-collisional rift volcanism of the Tianshan Mountains, northwestern China. Acta Geologica Sinica (English Edition) 77, 338–360.

Xia, L.Q., Xu, X.Y., Li, X.M., Ma, Z.P., Xia, Z.C., 2012. Reassessment of petrogenesis of Carboniferous-Early Permian rift-related volcanic rocks in the Chinese Tianshan and its neighboring areas. Geoscience Frontiers 3, 445–471.

Xiao, W.J., Han, C.M., Liu, W., Wan, B., Zhang, J.E., Ao, S.J., Zhang, Z.Y., Song, D.F., Tian, Z.H., Luo, J., 2014. How many sutures in the southern Central Asian Orogenic Belt: insights from east Xinjiang–West Gansu (NW China)? Geoscience Frontiers 5, 525–536.

Xiao, W.J., Windley, B.F., Allen, M.B., Han, C.M., 2013. Paleozoic multiple accretionary and collisional tectonics of the Chinese Tianshan orogenic collage. Gondwana Research 23 (4), 1316–1341.

Xiao, W.J., Zhang, L.C., Qin, K.Z., Sun, S., Li, J.L., 2004. Paleozoic accretionary and collisional tectonics of the Eastern Tianshan (China): implications for the continental growth of central Asia. American Journal of Science 304, 370–395.

Xiao, X.C., Tang, Y.Q., Feng, Y.M., Zhu, B.Q., Li, J.Y., Zhao, M., 1992. The Tectonics in the Northern Xinjiang and its Adjacent Area. Geological Publishing House, Beijing (in Chinese).

Xu, L.L., Chai, F.M., Li, Q., Zeng, H., Geng, X.X., Xia, F., Deng, G., 2014. Geochemistry and zircon U-Pb age of volcanic rocks from the Shaquanzi Fe-Cu deposit in east Tianshan mountains and their geological significance. Geology in China 41 (6), 1771–1790 (in Chinese with English abstract).

Xu, S.Q., Zhao, T.Y., Feng, J., Gao, Y.F., Tian, J.T., Yang, Z.F., Liu, D.Q., 2011. Study on regional metallogenic regularity of marine volcanic type iron ore in the east Tianshan of Xinjiang. Xinjiang Geology 29 (2), 173–177 (in Chinese with English abstract).

Xu, Y.G., Zhang, H.H., Qiu, H.N., Ge, W.C., Wu, F.Y., 2012. Oceanic crust components in continental basalts from Shuangliao, Northeast China: derived from the mantle transition zone? Chemical Geology 328, 168–184.

Yang, X.K., Ji, J.S., Luo, G.C., Tao, H.X., 1997. Plate tectonics and forming law of the metallic ore deposits in eastern Tianshan. Journal of Xi'an College of Geology 19 (3), 34–42 (in Chinese with English abstract).

Yang, X.K., Tao, H.X., Luo, G.C., Ji, J.S., 1996. Basic features of plate tectonics in east Tianshan of China. Xinjiang Geology 14 (3), 221–227 (in Chinese with English abstract).

Yuan, H.L., Gao, S., Liu, X.M., Li, H.M., Gunther, D., Wu, F.Y., 2004. Accurate U-Pb age and trace element determinations of zircon by laser ablation-inductively coupled plasma-mass spectrometry. Geostandards and Geoanalytical Research 28, 353–370.

Zhang, D.Y., Zhou, T.F., Yuan, F., Fan, Y., Deng, Y.F., Xu, C., Zhang, R.F., 2014. Genesis of Permian granites along the Kangguer Shear Zone, Jueluotage area, northwest China: geological and geochemical evidence. Lithos 198, 141–152.

Zeng, Z.G., Yu, S.X., Wang, X.Y., Fu, Y.T., Yin, X.B., Zhang, G.L., Wang, X.M., Chen, S., 2010. Geochemical and isotopic characteristics of volcanic rocks from the northern East China Sea shelf margin and the Okinawa Trough. Acta Oceanologica Sinica 29, 48–61.

Zhang, X.H., Huang, X., Chen, J.P., Liao, Q.A., Duan, X.F., 2012. Stratigraphical sequence of Carboniferous marine volcanic-deposit rock and its geological age in Jueluotage area, eastern Tianshan. Earth Science-Journal of China University of Geosciences 37 (6), 1305–1314 (in Chinese with English abstract).

Zheng, Y.F., 2012. Metamorphic chemical geodynamics in continental subduction zones. Chemical Geology 328, 5–48.

Zhou, T.F., Yuan, F., Zhang, D.Y., Fan, Y., Liu, S., Peng, M.X., Zhang, J.D., 2010. Geochronology, tectonic setting and mineralization of granitoids in Jueluotage area, eastern Tianshan, Xingjiang. Acta Petrologica Sinica 26 (2), 478–502 (in Chinese with English abstract).

Zhu, D.C., Pan, G.T., Mo, X.X., Liao, Z.L., Jiang, X.S., Wang, L.Q., Zhao, Z.D., 2007. Petrogenesis of volcanic rocks in the Sangxiu Formation, central segment of Tethyan Himalaya: a probable example of plume-lithosphere interaction. Journal of Asian Earth Sciences 29, 320–335.

Zhu, D.C., Zhao, Z.D., Niu, Y.L., Dilek, Y., Wang, Q., Ji, W.H., Dong, G.C., Sui, Q.L., Liu, Y.S., Yuan, H.L., 2012. Cambrian bimodal volcanism in the Lhasa Terrane, southern Tibet: record of an early Paleozoic Andean-type magmatic arc in the Australian proto-Tethyan margin. Chemical Geology 328, 290–308.

Zindler, A., Hart, S., 1986. Chemical geodynamics. Annual Review of Earth and Planetary Sciences 14, 493–571.